NTNU
Norwegian University of
Science and Technology

Time domain studies of training effects in Co/Cu/FeNi/FeMn spin valves

Kofi Tutu Addo Assuming-Gyimah

Condensed Matter Physics
Submission date: June 2011
Supervisor: Erik Wahlstrøm, IFY

Norwegian University of Science and Technology
Department of Physics

Faculty of Natural Science and Technology
Department of Physics

NTNU
Norwegian University of
Science and Technology

Master's thesis

Kofi Tutu Addo Assuming-Gyimah

Thesis started:	23.08.2010
Thesis submitted:	30.06.2011

Discipline: **Condensed Matter Physics**

Title: *"Time domain studies of training effects in Co/Cu/FeNi/FeMn spin valves"*

This work has been carried out at Department of Physics at the Norwegian University of Science and Technology, under the supervision of Erik Wahlström.

Trondheim, 30.06.2011

Erik Wahlström

Responsible supervisor

Associate Professor at Department of Physics

Time Domain Studies of Training Effects in Co/Cu/FeNi/FeMn Spin Valves

Kofi Tutu Addo Assuming-Gyimah

Abstract

The recovery and the relaxation behaviors of the exchange bias (H_E) in a Co/Cu/FeNi/FeMn spin valve has been studied via point contacts technique with high field scan rates ranging from 1050 to 13500 Oe/s. The evolution of the exchange bias with the number of field cycles (n) shows a $1/\sqrt{n}$ dependence as against $\ln(n)$ in a previous study. A recovery of the exchange bias when the field cycling is stopped has been observed and the recovery ratio (R) is found to be a function of the logarithm of the recovery time ($\log(t)$) in agreement with previous studies. The relaxation time (τ) of the exchange bias is estimated to be 6.62, 20.85, 43.10, 109.02, and 297.24 s for 13500, 5400, 2700, 1350, and 1050 Oe/s respectively. The $1/\sqrt{n}$ dependence of H_E and the $\log(t)$ dependence of R have been discussed using thermal activation model.

This work is dedicated to my parents, the rest of the family, and my friends.

Acknowledgments

I am wholeheartedly grateful to God, who made everything possible (from life, hope, trust, strength, understanding, to humility) towards the successful completion of my studies.

It is a pleasure to thank those who made this thesis possible. My first and innermost thanks go to my supervisor Erik Wahlsröm for not just being my supervisor but also for his patience and step-by-step guidance through MATLAB without which this work would have been next to impossible.

I also extend my web of thanks to Randi Holmestad (Professor at Department of Physics, NTNU and my course coordinator) and Snorre Hansen (Student Advisor in-charge of international students) for their support and guidance during the last two years. My unalloyed thanks is extended to Anette Moen, Executive Officer in charge of the Quota Scheme Program and all her colleagues at the NTNU International office for their diverse assistance through all this course. Also, to the Norwegian Government I say a big thank you for the scholarship opportunity to study here in Norway.

To my colleague Condensed Matter Physics students "The Condensers"; Muhammad "The Nano Indenter" Hanif, Godfred "The Godfather" Inkoom, "The Prince of Persia" Mohsen Dahesh, and Lamenew "The Ethiopian D" Azena Biaschile I say "Ayekoo".

It is an honour for me to thank my family for being there for me over the years; to my father who has always been my best friend and confidant, words are just not enough; to my mother who never run short of words of encouragement when the going gets tough for me, you are the definition of a mother; and to the rest of the family, I say "meda mo ase papaapa". I wish to express my sincere thanks to my "Every Friend Everywhere" [1]; your "social networking" has always done the trick.

Finally, to all who have contributed in diverse ways to bring this thesis to fruition, I say, "tusen takk".

Kofi Assuming-Gyimah

Trondheim, 30.06.2011

---

[1] EFE

Contents

Abstract . . . iii
Dedication . . . v
Acknowledgments . . . vii

1 Introduction **3**
1.1 Spintronics . . . 3
1.2 Layout of this work . . . 6

2 Background **7**
2.1 Ferromagnetism and antiferromagnetism . . . 7
  2.1.1 Ferromagnetism . . . 7
  2.1.2 Antiferromagnetism . . . 9
2.2 Band model of ferromagnetism . . . 11
2.3 Magnetic domains and domain walls . . . 13
  2.3.1 Domains and domain walls: what are they? . . . 13
  2.3.2 Energetics of a ferromagnet . . . 14
  2.3.3 Ferromagnetic domain formation and domain walls . . . 17
  2.3.4 Antiferromagnetic domains . . . 18
  2.3.5 Magnetization reversal and hysteresis . . . 19
2.4 Exchange bias and training effect . . . 20
  2.4.1 Exchange bias and unidirectional anisotropy . . . 20
  2.4.2 Training effect . . . 23
2.5 Interlayer exchange coupling . . . 24
2.6 Giant magnetoresistance effect . . . 25
  2.6.1 Phenomenological description . . . 25
  2.6.2 The microscopic picture: spin dependent scattering . . . 28
2.7 Spin transfer torque effect . . . 31
  2.7.1 The Landau-Lifshitz-Gilbert equation . . . 32
  2.7.2 The spin transfer term . . . 33
  2.7.3 Spin transfer torques in antiferromagnets . . . 34
2.8 Point contact measurements . . . 35

3 Experimental Setup and Method 37
3.1 Instrumentation . . . 37
3.1.1 Electromagnet and current source . . . 38
3.2 Sample . . . 38
3.3 Experimental method . . . 39

4 Results and Discussion 41
4.1 Giant Magnetoresistance . . . 41
4.2 Exchange bias and training effect . . . 42

5 Conclusion 51
5.1 Conclusion . . . 51
5.2 Suggestions for future work . . . 51

Bibliography 57

List of Figures

2.1 (a) Temperature dependence of the magnetization of a ferromagnetic material, dependence of the inverse of susceptibility, (b) the dependence of the magnetization on applied magnetic field; (c) schematic representation of ferromagnetism. After [17]. 7

2.2 Schematic representation of the temperature dependence of the (a) the magnetization of the opposing sublattices in an antiferromagnetic material, (b) with variation of the inverse susceptibility; (c) schematic representation of antiferromagnetism. After [17]. 9

2.3 Density of states for Fe, Co, Ni, and Cu. The Fermi level is set to zero. A simplified outline of the d and s bands are printed in red and blue in the Cu plot [22]. 12

2.4 Domains observed with magneto-optical methods on homogeneous magnetic samples. (a) Images from two sides of an iron whisker, combined to simulate a perspective view, (b) Thin film NiFe element with a weak transverse anisotropy, (c) Faraday effect picture of domains in a single-crystal garnet film with perpendicular anisotropy, with a schematic of the magnetization [25]. 13

2.5 Origin of domains: division of a single magnetic domain, minimizing the magnetostatic energy [30]. 18

2.6 a) Bloch domain wall and b). Néel domain wall in a planar film with the magnetization in the domain parallel to the film plane [13]. 18

2.7 Schematic representation of a hysteresis loop of a ferromagnetic material. The dashed curve is for virgin material [18]. 19

2.8 Hysteresis loop at 77 K of partially oxidized Co particles. Curve (1) shows the resulting loop after cooling the material in a 10 kOe field. Curve (2) shows the loop when the field is cooled to zero [33]. 20

2.9 Schematic diagram of the spin configuration of an FM-AFM bilayer (a) at different stages (i)-(v) of an exchange biased hysteresis loop (b). The spin configurations are just to illustrate the effect of the coupling of the FM and AFM magnetizations [34]. 21

2.10 Schematic diagram illustrating the phenomena of (a)antiferromagnetic coupling and (b) ferromagnetic coupling between two ferromagnetic layers separated by a spacer layer. The arrows show direction of magnetization. . . . 24

2.11 Normalized resistance versus applied magnetic field for several antiferromagnetically coupled Fe/Cr multilayer at 4.2 K. Arrows indicate the saturation field H_S, which required to overcome the antiferromagnetic interlayer exchange coupling between the Fe layers and align their magnetizations parallel. After [50]. 26
2.12 Schematic illustration of (a) the current in plane (CIP), (b) the current perpendicular to the plane (CPP) giant magnetoresistance geometry. After [1]. 27
2.13 Various structures in which GMR can be observed: magnetic multilayer (a), pseudo spin valve (b), spin valve (c) and granular thin film [50]. 28
2.14 The density of states of copper, cobalt and iron. Broken line denotes the position of the Fermi level [2]. 29
2.15 Band structures of (a) cobalt and copper along [001] direction in the vicinity of one of the Cu Fermi surface necks (b) iron and chromium in the [001[direction. Broken line denotes the position of the Fermi level [2]. 30
2.16 A resistor model of GMR [2]. 31
2.17 A schematic of spin-transfer model. (a) Electrons flowing from F_2 to F_1, initially polarized along the direction of magnetization $\hat{M}_{fixed}$, of F_2, exert torque on the magnetization $\hat{M}$, of F_1, which acts to align $\hat{M}$ with $\hat{M}_{fixed}$. (b) In the case of a current flowing in a reverse direction to (a), the electrons with spin antialigned with $\hat{M}_{fixed}$ will be reflected from F_2 and return to F_1 exerting a torque opposite to that in (a) which result in $\hat{M}$ turning away from $\hat{M}_{fixed}$. Antialigned configuration of the magnetizations is thus stable. After [56]. 33

3.1 A schematic diagram of the circuit used for measuring the contact resistance. 37
3.2 The experimental setup of the point-contact resistance measurement. The sample is placed on a rectangular acrylic platform in-between the two Helmholtz coils. The different parts of the setup are tightly held together so that the system acts as one unit. 39

4.1 Typical magnetoresistance curves obtained when a 4 A current was sent through the sample while being swept with a triangular wave at a field scan rate of 13500 Oe/s. 41
4.2 An H_E versus n where the magnetic field was turned off after $T_{on} = 5$ s for $T_{off} = 0.01$ s, then turned back on for another $T_{on} = 5$ s. 42
4.3 An H_E versus n where the magnetic field was turned off after $T_{on} = 5$ s for $T_{off} = 0.05$ s, then turned back on for another $T_{on} = 5$ s. 43
4.4 An H_E versus n where the magnetic field was turned off after $T_{on} = 5$ s for $T_{off} = 0.1$ s, then turned back on for another $T_{on} = 5$ s. 43
4.5 An H_E versus n where the magnetic field was turned off after $T_{on} = 5$ s for $T_{off} = 0.5$ s, then turned back on for another $T_{on} = 5$ s. 44
4.6 An H_E versus n where the magnetic field was turned off after $T_{on} = 5$ s for $T_{off} = 1$ s, then turned back on for another $T_{on} = 5$ s. 44
4.7 An H_E versus n where the magnetic field was turned off after $T_{on} = 5$ s for $T_{off} = 5$ s, then turned back on for another $T_{on} = 5$ s. 45

4.8 Exchange field H_E versus number of field cycles n. The red dash, blue dot, and brown dash-dot lines are respectively $e^{-\alpha n}$, $\ln(n)$, and $1/\sqrt{n}$ fits to the data. 46
4.9 Exchange field H_E versus number of field cycles $n^{-1/2}$. The data shows a reasonable adherence to this form. 46
4.10 The percentage recovery of the exchange field H_E as a function of the interval time (t_{off}) for different field scan rate. The solid lines are linear fits of a $\log(t_{off})$ function. 47
4.11 The slope and intercept of the fits in Figure 4.10 as a function of the field scan rates. The solid lines are linear fits to the logarithm of the field scan rate. 48

Chapter 1

Introduction

1.1 Spintronics

Definition and principle

In the words of Žutić *et al* [1] spin electronics[2] is a new field of research that relies closely on a long tradition of results obtained in diverse areas of physics; for example, magnetism, semiconductor physics, superconductivity, optics and mesoscopic physics, and establish new connections between its different subfields. The central objective of this multidisciplinary research field is the active manipulation of spin degrees of freedom in solid state systems which results in the manipulation, storage or transfer of information [1]. In other words, in spin electronics, the electron spin, in contrast to its charge in conventional electronics, carries information. This offers a way for the development of a new generation of devices that either exploits the electron spin alone or simultaneously exploits the charge and the spin [1, 2]. We can significantly enhance the performance of electronic devices by integrating the spin degree of freedom into conventional semiconductor charged-based electronics or exploiting the spin degree of freedom alone. These new devices have potential advantage of nonvolatility, high data processing speed, require less electric power, and will have increased integration densities compared to conventional semiconductor devices [3].

Spin is a fundamental characteristic quantum-mechanical property of elementary particles of which the electron is a member. It is the intrinsic angular momentum property of these particles. Since aligning electron spins bring about magnetism, the manipulation of the particles spin's phase coherence and charge dynamics can be used to manipulate magnetized domains and vice versa [1, 4].

---

[2] Also known as spintronics or magnetoelectronics.

Motivation and objectives

The enormous "contagious" interest spintronics has generated partly because of the "interesting physics" it presents and partly due to its potentially wide applications, has caught up with me too. From the application of the giant magnetoresistance (GMR) effect in read heads for magnetic disk to the possible application of spin transfer torque (STT) effect in STT-based MRAM, the study of spintronics phenomena like those mentioned above and others like exchange bias, interlayer coupling etc. is set to continue to generate a lot of interest for a long time to come.

Point contacts is one of the techniques via which the properties of magnetic materials at the nanoscale is studied. The study of the shape and size effects of the magnetic properties of nanostructures is a very active field of research [13]. In this thesis, the recovery and the relaxation behaviors of the exchange bias in Co/Cu/FeNi/FeMn spin valves is studied via point contact technique by driving a constant current through the contact junction while sweeping the structure with an external magnetic field.

The technical basis of spintronics

Mott laid the technical foundation of spin electronics in his attempt to explain the anomalous resistivity exhibited by doped ferromagnetic (FM) materials [5]. He observed that the resistance of metallic ferromagnets did not obey Matthiesen's rule as in nonmagnetic metals but their behavior was dependent on the dopant. Mott realized that as magnon scattering diminished at sufficiently low temperatures, electrons of majority and minority spin, with magnetic moment aligned parallel (spin up) and antiparallel (spin down) relative to the magnetization orientation of the ferromagnet, respectively do not mix during scattering [1, 5]. That is, though spin-flip scattering does occur, they are rare and can therefore be neglected because of the brief timescale defined by all other processes in the system. He therefore proposed a "two current model" based on the fact that the parallel and antiparallel spin electrons have unequal contributions to conductivity and hence can be considered as a two separate currents [5]. Again the densities of states, and consequently the mobilities of the two channels are different as a result of exchange bias leading to difference in the number of occupied states at the Fermi level. This causes the currents to have different conductivities and hence the conductivity of the ferromagnet is expressed as the sum of two independent and unequal parts for the two different spin projections [1]. If the polarization, that is the number of carriers with spin up or spin down is not equal to one, the current is said to be spin-polarized.

Giant magnetoresistance effect

The discovery of giant magnetoresistance (GMR) effect in 1988 [6] marked the first practical application of spintronics [7]. The GMR is a quantum mechanical effect observed in layered magnetic thin-film structures that is composed of alternating ferromagnetic and nonmagnetic layers [4, 7]. In the most basic application of GMR effect, usually referred to as the "spin valve", two ferromagnetic layers are separated by a thin nonmagnetic spacer layer. The resistivity of the structure is found to be lowest when the magnetic moment (i.e., the magnetization) in the two ferromagnetic layers are aligned (parallel) and have the highest value when they are anti-aligned (antiparallel). This observation is due to the fact that spin-aligned currents from one layer experience significant (maximum) scattering when they encounter an oppositely aligned magnetic layer. This scattering creates additional resistance resulting in an increase in the resistance of the material. On the contrary, when the magnetic fields in the layers are aligned in the same direction, the spin-aligned current passes through with minimum scattering [4, 7]. For such a GMR structure, there is significant change in the electrical resistance when a small external magnetic field is applied. The effect was found to be much larger than other known magnetoresistance effects and as a result the name "giant". GMR was discovered by an IBM research group led by Peter Grünberg [Binasch *et al.* [8]], and simultaneously but independently by another group at the university of Paris-Sud led by Albert Fert [Baibich *et al.* [6]]. They were jointly awarded 2007 Nobel Prize in physics [4].

The first commercial product based on GMR effect was the magnetic field sensor and was available on the industrial market in 1994. The GMR-based read head for magnetic disk drives [4, 7] developed by IBM in 1997 was the first GMR-based technology to have major economic success [7]. The rapid increase in magnetic storage densities recorded in recent times is largely attributed to this technology [4].

Spin-transfer torque effect

As opposed to GMR in which the flow of spin-polarized (spin-aligned) current is affected by the relative orientation of the magnetizations in the ferromagnetic layers [9], Slonczewski [10] and Berger [11] independently predicted an important reverse phenomenon in 1996. In this effect, spin-polarized currents can transfer spin angular momentum from carriers to a ferromagnet, and this causes a re-orientation of the magnetization of the ferromagnet, even in the absence of an applied field [1, 9, 12]. This effect, called Spin-Transfer Torque (STT), has today stimulated intense theoretical and experimental research in spintronics [1, 9]. The spin transfer phenomenon occurs when an electron current flows through two ferromagnetic layers separated by a non magnetic spacer layer. The first ferromagnetic layer (F_1) is considered as fixed and serves as a spin polarizer while the second ferromagnetic layer (F_2) is free to move under the action of the current. As the current passes (via transmission or reflection) from F_1 it becomes spin-polarized and it usually remains in this state as it traverses the nonmagnetic spacer layer and enters and interacts with F_2. A torque is generated on the magnetic moment of F_2 through the transfer of angular momentum from the spin-polarized current to the F_2 magnetization during the interaction. If the spin-polarized current is of sufficient strength, the torque can oppose the intrinsic damping of F_2 inducing magnetization precession and, or reverse the magnetization direction [12, 14]. This theoretical prediction has been verified experimentally by Tsoi *et al.* [15] and Myers *et al.* [16] in 1998 and 1999 respectively. Potential application of STT effect includes STT-based magnetic random access memory (MRAM) and current tunable high-frequency oscillators by spin wave generation [12].

1.2 Layout of this work

The work is divided into five chapters. In chapter 1 (this chapter), a brief introduction of spintronics is presented. The theoretical background of the experiment including spintronics phenomena like exchange bias (§ 2.4) and spin transfer torque effect are (§ 2.7) in discussed in chapter 2. Chapter 3 is dedicated to the experimental setup and method while experimental results are presented and discussed in chapter 4. The conclusion and suggestion for future work is presented in chapter 5.

Chapter 2

Background

2.1 Ferromagnetism and antiferromagnetism

2.1.1 Ferromagnetism

Ferromagnetism is characterized by spontaneous magnetization in small domains below the Curie temperature (T_c) as a result of a spontaneous parallel alignment of atomic magnetic moments, with long range order (figure 2.1(c)) [17, 18].

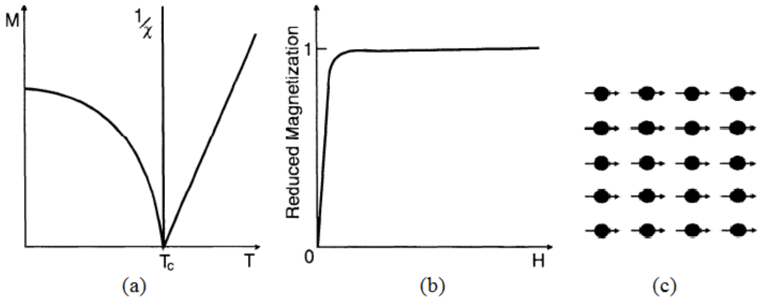

Figure 2.1: (a) Temperature dependence of the magnetization of a ferromagnetic material, dependence of the inverse of susceptibility, (b) the dependence of the magnetization on applied magnetic field; (c) schematic representation of ferromagnetism. After [17].

The ferromagnetic order, that is, the spontaneous polarization disappears above the Curie temperature. The material, at this point, is paramagnetic [17–19] and the magnetic susceptibility (Figure 2.1(a)) obeys the Curie-Weiss law [20]

$$\chi = \frac{M}{H} = \frac{C}{T - C\gamma} = \frac{C}{T - \theta}, \tag{2.1}$$

where C is the Curie constant, and the quantity $\theta(=\gamma C)$ is the measure of the strength of the interactions between the individual magnetic moments since it is proportional to the molecular field constant γ (to be discussed next). It has dimensions of temperature and it is constant for a particular substance. For substances that obey Curies law $\theta = \gamma = 0$ [19]. Example of ferromagnets (FM) are iron (Fe), nickel (Ni), cobalt (Co), and gadolinium (Gd) [17, 18].

Molecular field theory

The molecular field model, proposed by Weiss, assumes an average field at a given temperature while neglecting the possible fluctuations that may occur in it [21]. A molecular field (H_m) is responsible for the parallel alignment of magnetic moments. A ferromagnet is therefore seen as a paramagnet with a very large molecular field [18], the magnitude of which is proportional to the magnetization [18, 19, 21]

$$H_m = \gamma M, \tag{2.2}$$

where

$$\gamma = \frac{1}{N}\sum_{j\neq 1} n_{ij}, \tag{2.3}$$

is the molecular field constant and N is the number of atoms per unit volume. The molecular field has the same effect as the applied field with the latter usually being smaller. The alignment of magnetic moments that is achieved with an applied field at low temperatures is realized with the molecular field at high temperatures; for instance, higher than room temperature in the case of ferromagnets [21]. The numerical values of the molecular field is estimated to be 10^9 A/m (10^7 Oe) [18].

As stated already, since the molecular field and the externally applied field have the same effect, the molecular field helps the applied field in magnetizing the material [19]. We therefore replace H in the Curie-Weiss law with [17, 20, 21]

$$H^i = \gamma M + H. \tag{2.4}$$

H^i has to be large enough to be able to induce spontaneous magnetization at room temperature. The paramagnetic susceptibility above T_c is [20]

$$\chi = \frac{C}{T - \theta_p}, \tag{2.5}$$

where

$$\theta_p = T_c = \frac{\mu_0 \gamma n g^2 \mu_B^2 J(J+1)}{3k_B}, \tag{2.6}$$

where μ_0 is the magnetic constant, n is the number of magnetic atoms per unit volume, g is the Landé-factor, μ_B is the Bohr magneton, J is the total angular momentum quantum number, and k_B is the Boltzmann constant.

The susceptibility diverges at the point where the paramagnetic Curie temperature (θ_p) becomes equal to the Curie temperature (T_c) [20] and the spontaneous magnetization of the ferromagnet disappears [21].

2.1.2 Antiferromagnetism

Antiferromagnetism is characterized by a spontaneous antiparallel alignment of atomic magnetic moments which results in a zero net magnetization (Figure 2.2(c)) [17].

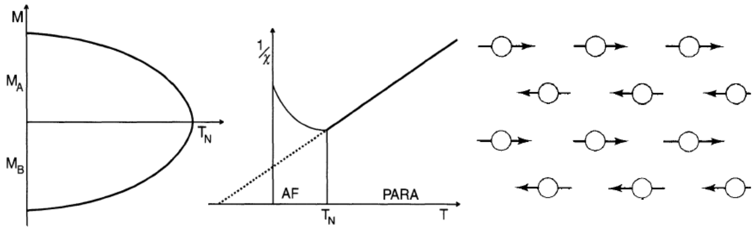

(a) (b) (c)

Figure 2.2: Schematic representation of the temperature dependence of the (a) the magnetization of the opposing sublattices in an antiferromagnetic material, (b) with variation of the inverse susceptibility; (c) schematic representation of antiferromagnetism. After [17].

Antiferromagnetism usually exist at a sufficiently low temperatures and it disappears above a critical temperature called the Néel temperature (T_N). Above T_N antiferromagnets (AFMs) usually become paramagnets [18] and the inverse of the susceptibility follows a linear dependence, that is, $T = f\left(\frac{1}{\chi}\right)$ law represented by figure 2.2(b) [17, 18]. At temperatures lower than T_N, however, the magnetic susceptibility may rise with decreasing temperature [18]. A negative θ is obtained when the paramagnetic line is extrapolated to $1/\chi = 0$ [18, 19]. The equation of the paramagnetic line is therefore [19]

$$\frac{1}{\chi} = \frac{T + \theta_p}{C}, \tag{2.7}$$

$$\chi = \frac{C}{T + \theta} = \frac{C}{T - (-\theta_p)}. \tag{2.8}$$

We can infer from Eq.(2.8) that antiferromagnetic materials obey the Curie-Weiss law but with a negative value of θ_p [18, 19]. Example of antiferromagnetic materials are FeO, Fe_3Mn, MnO, and NiO [17, 18]. a-Mn is an itinerant AFM and does not obey the Curie-Weiss law [17].

Molecular field theory

Let us consider the simplest possible case of the molecular field theory, in the form of a Néel ferromagnet, which has two identical and oppositely directed magnetic sublattices A and B, such that an ion A has only B ions as nearest neighbors, and vice versa. Again let the magnetizations of the sublatices be $M_A = -M_B$ [19, 20] (Figure 2.2(a)). The molecular fields acting on each sublattice are [20]

$$H_A^i = \gamma_{AA} M_A + \gamma_{AB} M_B + H, \tag{2.9}$$

$$H_B^i = \gamma_{BA} M_A + \gamma_{BB} M_B + H, \tag{2.10}$$

where $\gamma_{AA} = \gamma_{BB}$, $\gamma_{AB} = \gamma_{BA}$, and H is the contribution from the externally applied field. The negative Weiss coefficient γ_{AB} accounts for the intersublattice molecular field coupling, and γ_{AA} is included to represent the intrasublattice field interactions [20]. Equations (2.9) and (2.10) are valid for both above and below T_N. Above T_N, which is in the paramagnetic region, the susceptibility when we assume a Curie-Weiss behavior is [20]

$$\chi = \frac{M_A + M_B}{H} = \frac{C}{T - \theta_p}. \tag{2.11}$$

Here,

$$C = 2C', \quad \theta_p = C'(\gamma_{AA} + \gamma_{AB}). \tag{2.12}$$

Equations (2.8) and (2.11) are equivalent. The values of γ_{AA} and γ_{AB} can be evaluated from the known values of T_N and θ_p. Also, the paramagnetic temperature is often negative since $\theta_p < T_N$ for $\gamma_{AB} < 0$ [20].

When a field is applied above T_N, each sublattice becomes magnetized in the direction of the field, and subsequently sets up a molecular field which is opposite the direction of the applied field, and which tend to reduce both M_A and M_B. This results in smaller susceptibility χ, and larger $1/\chi$, than that of an ideal paramagnetic in which molecular field is zero [19].

At a temperature infinitesimally below T_N, since saturation effects are unimportant near T_N, M is assumed to be still proportional to total field and therefore Eq.(2.9) and (2.10) are still valid. At $T = T_N$ and $H = 0$, we obtain from Eq.(2.9) and (2.12)

$$\rho C^{'} \gamma = \theta_p = \left(\frac{M_A}{M_B}\right) T_N. \tag{2.13}$$

The Néel temperature, at which the maximum in the $\chi - T$ curve occurs, should therefore equal the θ_p value found from the high-temperature susceptibility measurement [19].

2.2 Band model of ferromagnetism

The properties of magnetic metals are not simply explained by considering the atomic picture of magnetic interactions. The discrete electronic energy levels are smeared out into bands when atoms are bonded in a periodic lattice and this is found to influence the magnetic moments [22]. One would expect that electrons occupying unfilled core levels would interact via Heisenberg mechanism resulting in ferromagnetism. Also, the conduction process in these metals would be due to electrons in much high bands and that there was little interaction between the ferromagnetic and the conducting electrons [23]. However, this is not always the case. The spontaneous magnetization that defines the ferromagnetic property of transitional metals Fe, Ni and Co is best understood within the context of electron bands often referred to as the “band model” of ferromagnetism [22].

The charge- and spin transport properties of Fe, Ni and Co have their origin in the 3d and 4s electrons. The 4s electrons are largely shielded from the atomic potential and are well described with “nearly free electron” model which predicts large group velocity and parabolic energy bands. The electrons in the 3d bands are more tightly bound to the core and delocalization is explained by “hopping” between atoms in a “tight binding model”. The tight binding model predicts narrower bands and lower mobility compared to the nearly free electron model. There is a hybridization of the 4s and 3d states near the Fermi level to form mixed states of s and d and these states partake in both charge transport and magnetic moment. They are referred to as *itinerant* d-electrons [22].

Figure 2.3 shows the plots of the calculated electron states for Fe, Ni, Co and Cu. The ferromagnetic metals, Fe, Ni and Co, have different density of states (DOS) associated with them at the Fermi level for spin-up and spin-down electrons and the shift in DOS for two spin populations is a result of exchange splitting. This is as a result of the different filling of the spin-up and spin-down bands. The movement of electrons from a down- to an up-spin band from a paramagnetic state is at the expense of energy. An excess of spin up electrons results in a net magnetization which create an exchange field in the solid. This lowers the energy of the spin up electrons whiles increasing that of the spin down electrons. Spontaneous exchange splitting is energetically favored if:

$$U.DOS(E_F) \geq 1 \tag{2.14}$$

$DOS(E_F)$ is the density of states at the Fermi level and U is a measure of the Coulomb; proportional to the exchange interaction [22]. Equation (2.14) is the so-called *Stoner*

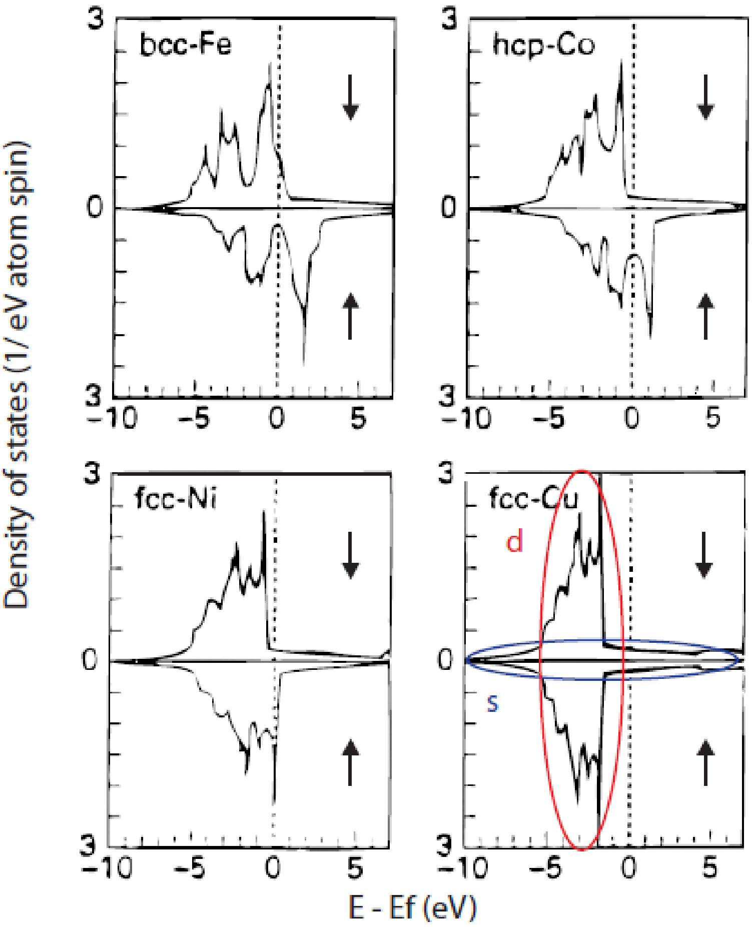

Figure 2.3: Density of states for Fe, Co, Ni, and Cu. The Fermi level is set to zero. A simplified outline of the d and s bands are printed in red and blue in the Cu plot [22].

criterion for the existence of ferromagnetism.

The model presented above correctly predicts the existence of ferromagnetism only in Fe, Co and Ni. The spin moments of Fe, Co and Ni are $2.2\mu_B$, $1.6\mu_B$ and $0.6\mu_B$ respectively. In the case of elements in the 4d series, the value of Eq.(2.14) is to small too achieve a ferromagnetic state [20].

2.3 Magnetic domains and domain walls

2.3.1 Domains and domain walls: what are they?

Definition

The macroscopic properties of a magnetic material are explained by the magnetic microstructure [24]. Magnetic domains; regions of uniform magnetization, and magnetic domain walls; regions of transition between one domain in a given direction and another in a different direction, are the elements of the magnetic microstructure [13, 24] and are observed to appear spontaneously within an otherwise unstructured samples [25]. In other words, by alternating the direction of magnetization of a magnetized material with respect to the surface, the energy in the static magnetic fields surrounding the finite, magnetized material can be minimized. There are many types of domains depending on the magnetic history and the dominant energy contribution, and these differences are exploited in applications such as magnetoresistance from striped domains or high-density memory storage in magnetic bubble [13]. Figure 2.4 shows the magnetic microstructure of different magnetic samples. The directions of magnetization in the domains are indicated by arrows.

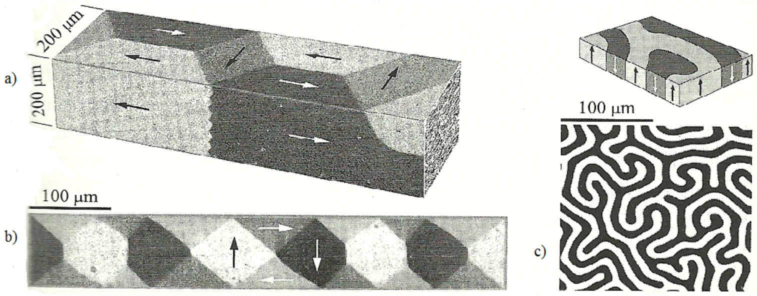

Figure 2.4: Domains observed with magneto-optical methods on homogeneous magnetic samples. (a) Images from two sides of an iron whisker, combined to simulate a perspective view, (b) Thin film NiFe element with a weak transverse anisotropy, (c) Faraday effect picture of domains in a single-crystal garnet film with perpendicular anisotropy, with a schematic of the magnetization [25].

Brief history

The term “domain” does not appear in literature until later although it was first considered by Pierre Weiss in 1906 when he suggested its existence in ferromagnets in his advance hypothesis of molecular field [13, 19]. Domains were an abstract construction used to explain [13]:

1. that even far below the Curie temperature, the total magnetization of a magnet is not the same as its saturation magnetization;
2. that a permanent magnet can be made from a ferromagnetic material by applying a

magnetic field;

3. the presence of hysteresis in the magnetization curve and the necessity of a coercive field to remove any net magnetization and
4. that ferromagnetic materials can simultaneously have zero and non-zero local magnetization.

It was the works of Sixtus and Tonks, and Bitter in the 1930's which fully confirmed Weiss's theory; consequently, Landau and Lifshitz proposed in 1935 that, domains emanate from the minimization of the magnetostatic energy resulting from the magnetic dipole interaction [13, 25].

2.3.2 Energetics of a ferromagnet

The micromagnetic theory is a phenomenological description of magnetism on a mesoscopic length scale that is employed in modeling the non-uniform spatial distribution of local magnetization $M(r)$. The theory is based on a variational principle which was developed within the framework of continuum mechanics [25–27]; it involves the minimizing the total free energy (E_{tot}) of a system. The maximum of the local magnetization is the spontaneous magnetization (M_s) and the unit magnetization vector is fixed to ensure that the total free energy attains an absolute or relative minimum when constrained by $m^2 = 1, where m is the vector field of the magnetization directions$ [25, 26].

Under equilibrium conditions, the magnetization of a sample aligns itself in the direction of an effective field which vary as a function of position. The energy components that make up this effective field include the externally applied (Zeeman) field, magnetocrystalline anisotropy, micromagnetic exchange, magnetoelastic interaction, and the magnetostatic field [27]. These energy components are divided into local and non-local energy terms. The local energy terms is made up of energy densities given by the local values of magnetization direction. The anisotropy energy, Zeeman energy, and magnetoelastic interaction energy are local functions of the magnetization direction. Exchange energy is also considered as local since it also dependent on the magnetization directions. The nonlocal energy components, which includes magnetostatic self-energy and stray field energy, produce torques on the magnetization vector that depend, at any point, on the magnetization direction at every other point[25, 27]. The major contributions to the total free energy of a ferromagnetic system are briefly treated.

Exchange energy

The exchange energy (E_{ex}) is the largest magnetic interaction and it is responsible for the spin system [24]. It is the energy required to rotate one atomic spin with respect to its neighbors, overcoming Pauli principle which tends to align the magnetic moments parallel in the case of ferromagnets and antiparallel for the antiferromagnetic case [13].

In other words, the exchange energy is responsible for magnetic ordering and spontaneous magnetization in ferromagnetic materials [24]. Direct exchange interaction results from different interactions such as spin-spin, spin-orbit, etc. The spin-spin interaction resulting from symmetry rules and orbit overlap can be written quantum mechanically as [13, 28]

$$E_{ex} = -JS_1S_2 \tag{2.15}$$

where J is the exchange parameter, and S_j is the spin of the electron. The classical expression, Eq.(2.15), differs from the Eq.(2.16) by a factor of 2 which is as a result of double counting over the atomic spins

$$E_{ex} = -\sum_{i>j} 2J_{ij}S_i.S_j \tag{2.16}$$

where J, in this instance, is the exchange integral linking the ith atom having spin S_i, to the jth atom with spin S_j [13]. The energy per unit area for a specific crystal lattice, when only second nearest neighbor interactions are taken into consideration, is [13]

$$E_{ex} = \int_{-\infty}^{\infty} \frac{JS^2}{a}(\nabla M)^2 dr^3 = A\int_{-\infty}^{\infty}(\nabla M)^2 dr^3 \tag{2.17}$$

where $A = \frac{JS^2}{a}$ is a material property-dependent exchange parameter referred to as the exchange stiffness constant, and a is the lattice constant [13, 25]. The probability of an individual spin flipping is proportional to

$$e^{E_{ex}/k_BT} \tag{2.18}$$

The probability is small for a ferromagnetic material at room temperature, when the measurement is made at low temperatures. In this case, the exchange energy results in a characteristic exchange length over which it is energetically favorable for all the magnetic moments to be aligned in the material [13].

Magnetocrystalline anisotropy energy

The energy of a ferromagnet depends on the direction of the magnetization relative to the structural axes of the material. The anisotropy energy (E_{an}) describes this dependence which results from spin-orbit interaction [25]. This energy originates from the coupling between spin moments and the electron orbital moment ($L-S$ coupling) and their coupling to anisotropic crystal field of a ferromagnet [13, 28]. It is the energy required to rotate the entire magnetization vector of particle from the easy direction into the hard direction [24] without displacing it or changing the relative orientation between spins [13, 28]. The energy is minimized when the magnetic moments are in the direction of the easy axes determined by the symmetry of the crystal. On the other hand, when the magnetic moments are along other directions, referred to as the hard axes, the energy is maximized [13]. The magnetic anisotropy energy density therefore remains constant when the magnetization is inverted which implies that the energy density is an even function of the the angle the magnetization (M) makes with the magnetic axes,

$$E_{an} = K_1 \sin^2 \gamma + K_2 \sin^4 \gamma + K_3 \sin^6 \gamma + ..., \tag{2.19}$$

where K_i is the magnetocrystalline anisotropy constant along the ith direction and γ is the angle M makes with the magnetic axes [24]. The anisotropic energy density of cubic crystal is given by [13, 25]

$$E_{an} \approx K_1[m_1^2 m_2^2 + m_1^2 m_3^2 + m_2^2 m_3^2] + K_2 m_1^2 m_2^2 m_3^2, \tag{2.20}$$

where m_i is the components of the magnetization along the cubic axes. The anisotropic constant is found to have a strong temperature dependence [29]. The K_1 has values in the range of $\pm 10^4$ Jm^{-3} for different materials, and K_2 and higher-order terms are often neglected [25]. The ratio of exchange energy to anisotropic energy is approximately $10^{-5} - 10^{-3}$ with exchange energy dominating [13].

Magnetostatic self-energy

This energy is associated with the elastic interactions between regions magnetized along the different axes [25] and dominates domain formation [13]. Free space magnetic dipoles are created in each single domain resulting in stray fields, hence magnetostatic energy. From Maxwell's equations

$$\nabla . B = \nabla .(\mu_0 H + M) = 0 \tag{2.21}$$

$$\nabla . H_s = -\nabla \big(M/\mu_0 \big) \tag{2.22}$$

where H_s is the stray field generated by the divergence of the magnetization field [13]. We can therefore calculate magnetostatic energy (E_{ms}) as [13]

$$E_{ms} = \frac{1}{2}\mu \int_{allspace} H_d^2 dV = \frac{1}{2} \int_{sample} H_d M dV \tag{2.23}$$

Zeeman energy

The Zeeman energy (E_{Ze}) is as a result of the interaction between the magnetic moments (magnetization) of a material and the external magnetic field [13, 24, 25] and it is given as

$$E_{Ze} = -\mu_0 \int H_{ext}.M dV \tag{2.24}$$

where H_{ext}, is the externally applied field. The Zeeman energy is dependent on only the average magnetization of the sample and not the particular domain structure or sample shape, in the case of uniform external field [13, 25].

Magnetoelastic energy

This energy results from the deformation experienced by a magnetic body when under the influence of a magnetic interaction. The effect of this energy in ferromagnets is small compared to all the other already discussed sources of energy [13].

2.3.3 Ferromagnetic domain formation and domain walls

The direction of magnetization of a sample would have been in one of the sample's easy axes if it was dependent only on the anisotropy energy and exchange energy; a sample homogeneously magnetized along an easy axis minimizes exchange energy and anisotropy energy but generates a magnetostatic energy depending on its physical shape [13, 17, 24]. The magnetostatic energy is as a result of the uncompensated surface magnetic poles (Figure 2.5a) which creates demagnetization fields. The multiple domains (Figure 2.5b) in the sample results from the minimization of the surface demagnetization fields, further subdivision of the domain would result in corresponding reduction in the surface demagnetization fields (Figure 2.5c); eventually reduced to zero by the formation of closure domains (Figure 2.5d) with magnetization perpendicular to that of the other domains [13, 17, 30]. The transition from one direction of spontaneous magnetization (i.e., domain) into another occurs in the domain walls [13]. In other words, ferromagnetic domains arise from the minimization of the stray field energy; the sample disintegrate into domains if the field energy is larger than the energy required to form the domain walls [24].

The formation of the domain walls also cost energy since the deviation of the magnetization involves exchange, anisotropy, magnetostatic, Zeeman, and magnetoelastic energy. The reduction in the demagnetization energy balances the energy required to form a wall; the width of the domain wall is determined by this same competition [13]. At or within the wall, the magnetization changes direction from one crystallographic direction to another. The continues variation of magnetization direction cost less energy than the abrupt transition [13, 19]. We discuss the two resulting prominent types of domain walls; *Bloch walls* and *Néel walls* [13, 24], named after the scientist who first conceived them.

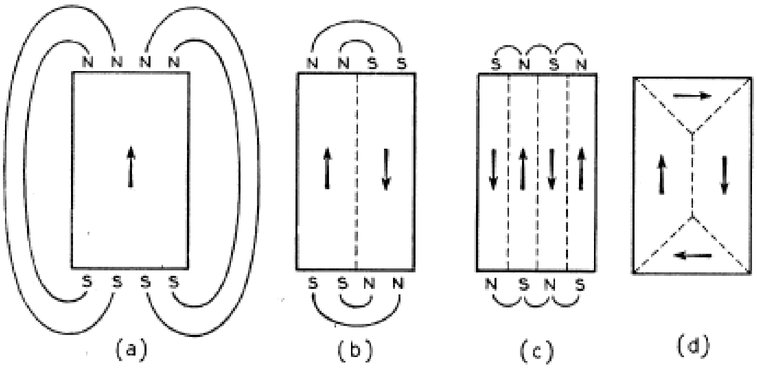

Figure 2.5: Origin of domains: division of a single magnetic domain, minimizing the magnetostatic energy [30].

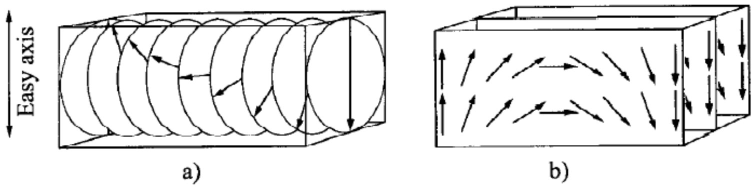

Figure 2.6: a) Bloch domain wall and b). Néel domain wall in a planar film with the magnetization in the domain parallel to the film plane [13].

If the plane of the wall contains the anisotropy axis, then the magnetization of the domain is parallel to the wall. When the magnetization is rotated parallel to the wall, then the component of the magnetization perpendicular to the wall is the same in both sides and the stray field attains its minimum value (zero). This is referred to as a Bloch wall [13] (Figure 2.6a). In other words, in a Bloch wall, a continuous 180-degree transition of magnetization occurs with the movements in the walls oriented parallel to the plane of the wall [24]. On the other hand, when the magnetization does not rotate parallel to the wall and as a result the component of the magnetization perpendicular to the wall changes during rotation, it is referred to as Néel wall [13] (Figure 2.6b). Hence in the Néel wall, the moments in the transition region are aligned perpendicular to the plane of the wall [24]. Bloch walls are energetically favorable in bulk-like thin films while Néel walls preferable in thin films and in applied fields [13, 24].

2.3.4 Antiferromagnetic domains

In the absence of magnetostatic energy in antiferromagnets [21, 24], magnetic domains are accounted for by the imperfections in the crystalline structure of a sample [24]. Thin films grown by epitaxial methods have imperfection or boundaries resulting in breaks in long-range magnetic ordering. The break in magnetic ordering causes a change of the spin axis [24]. As a result, the formation of antiferromagnetic domains does not cause a minimization of the free energy of a sample [21]. Unlike ferromagnetic domains, antiferromagnetic domains do not have much practical applications although most of the physical properties of the antiferromagnet depends on its domain structure [31]. Recent interest in antiferromagnetic domains have been boosted by the use of antiferromagnetic thin films in exchange bias applications; ferromagnetic-antiferromagnetic coupling which is exploited in GMR devices [21, 32]. Example of antiferromagnetic domains are the S (as in spin) domain and the T (as in twin) domain [21, 24].

2.3.5 Magnetization reversal and hysteresis

A magnetization curve (MC) result from the response of a magnetic material to an externally applied field. The knowledge of the MC is essential to all applications of magnetic materials. When a sample is subjected to an externally applied magnetic field, a torque $T = M \times H$ acts on the magnetization with corresponding changes in the magnetic microstructure in other to reduce energy. Regions in the microstructure where the magnetization is favorably aligned tends to increase in sizes at the expense of the unfavorably aligned ones through domain wall movement. The magnetization of the sample will eventually rotate to follow the applied field's direction. The MC usually depends on the initial distribution of magnetization over the sample volume i.e the sample's magnetization history [24].

Let us now consider a typical MC shown in the Figure 2.7. The magnetization increases with the field from the origin where the sample is considered unmagnetized (virgin material) until the magnetization reaches its maximum. The magnetization reaches a constant values at this point and this is referred to as the *saturated magnetization,* (M_s). The *saturation field* is the applied field at which the domain structure is removed and the magnetization direction follows that of the field.

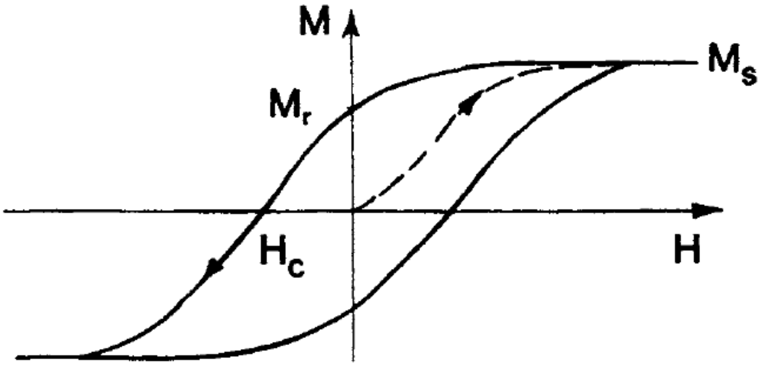

Figure 2.7: Schematic representation of a hysteresis loop of a ferromagnetic material. The dashed curve is for virgin material [18].

When the external field is reduced to zero, the sample's magnetization does not vanish; the sample continues to possess a positive magnetization called *remanent magnetization,* (M_r). This is the magnetization that is utilized in permanent magnets. In other to bring the magnetization to zero, a field is applied opposite the direction of the saturation field. The oppositely applied field is referred to as the *coercive field,* (H_c). Solids having a large combination of M_r and H_c (i.e., having a large loop area) are called hard magnetic materials whilst materials with a small loop area are referred to as soft magnetic materials. A further increase in the field in the opposite direction increases the magnetization in that direction. The loop is completed by reversing the applied field. [18, 19, 24]. This complete cycle through positive and and negative $H-$values, as shown in Figure 2.7, is referred to as a *hysteresis loop* [18].

2.4 Exchange bias and training effect

2.4.1 Exchange bias and unidirectional anisotropy

Exchange bias effect is observed when materials with ferromagnetic (FM)-antiferromagnetic (AFM) interfaces are cooled through the Néel temperature of the AFM; usually lower than the Curie temperature of the FM, which introduces an anisotropy in the FM [33–38]. It is one of the phenomena associated with exchange anisotropy which occurs at the FM-AFM interface [34] and was first observed in cobalt (Co)-cobaltous oxide (CoO) system by Meiklejohn and Bean in 1956 [33–37]. The phenomenon has since been observed in many different FM-AFM interfaces system such as small particles and inhomogeneous materials, FM films on AFM single crystals and thin films [34, 37]. Exchange bias and related effects have also been observed in other interfaces involving ferrimagnet-antiferromagnet and ferrimagnet-ferromagnet [34].

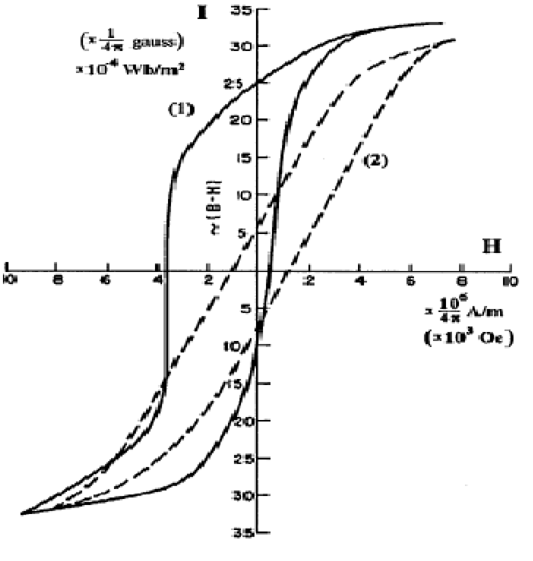

Figure 2.8: Hysteresis loop at 77 K of partially oxidized Co particles. Curve (1) shows the resulting loop after cooling the material in a 10 kOe field. Curve (2) shows the loop when the field is cooled to zero [33].

Meiklejohn and Bean used a compact fine particles of Co (10-100 nm) coated with CoO; i.e., particle consisted of a core single-domain FM Co with a shell of AFM CoO. The nanoparticles exhibited a normal symmetric hysteresis loop when cooled below room temperature (77 K) in the absence of an applied field. On the other hand, the center of the hysteresis loop of the Co shifts from its normal position at $H = 0$ to $H_E \neq 0$ along the field axis after cooling to a temperature of 77 K in an applied field (figure 2.8) [33, 34, 36, 37]. They attributed the shift to an interface coupling between the FM Co and the AFM CoO due to exchange anisotropy [34, 37]. The shift is generally referred to as "exchange bias" [37] and the amount of shift is quantified by the exchange bias field (H_E) as obtained by Meiklejohn [33, 34, 36]

$$H_E = \frac{\Delta\sigma}{M_{FM} t_{FM}} = \frac{2 J_{ex} S_{FM} S_{AFM}}{a^2 M_{FM} t_{FM}}, \tag{2.25}$$

where $\Delta\sigma$ is the interfacial exchange energy density, J_{ex} is the exchange interaction parameter, M_{FM} is the net ferromagnet magnetization, t_{FM} is the thickness of the ferromagnet, S_{FM} and S_{AFM} are the spins of the atoms of the of the ferromagnet and antiferromagnet respectively, and a is the lattice parameter.

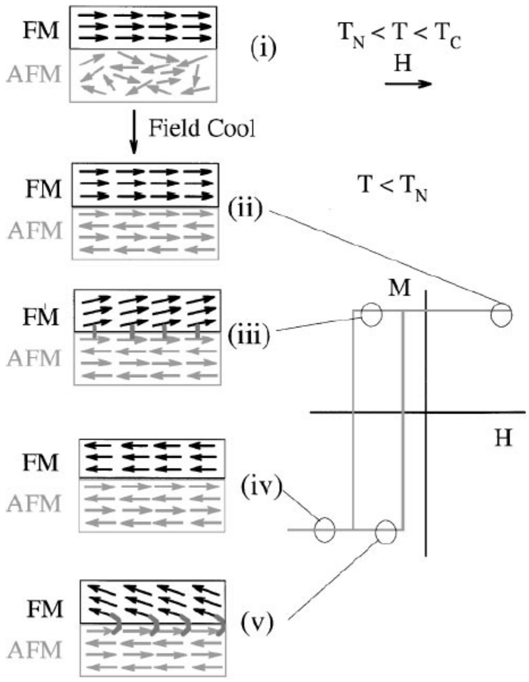

Figure 2.9: Schematic diagram of the spin configuration of an FM-AFM bilayer (a) at different stages (i)-(v) of an exchange biased hysteresis loop (b). The spin configurations are just to illustrate the effect of the coupling of the FM and AFM magnetizations [34].

Exchange bias can be understood qualitatively by assuming an exchange interaction at the FM-AFM interface. This approach gives an intuitive picture of the exchange bias at the macroscopic scale. In order to obtain a preferred direction of the coupling, the Curie temperature (T_c) of the FM is usually greater than the Néel temperature (T_N) of the AFM. We consider Figure 2.9, a schematic diagram of an FM-AFM bilayer to illustrate the different stages of the exchange bias. In the presence of a static saturated magnetic field in the temperature range, $T_N < T < T_c$ of a ferromagnet, the FM spins follow the field direction while the AFM spins remain paramagnetic and have random direction (Figure 2.9(i)). As the temperature of the system is lowered through $T < T_N$ in the presence of the field, the AFM spins next to the FM align ferromagnetically in the case of a ferromagnetic exchange coupling; i.e., the AFM spins couples to that of the FM spins and points in the same direction as a result of interaction at the interface. The next spin plane in the AFM also orders opposite to the direction of the first spin plane and the rest of the spin planes follow the AFM order giving rise to a zero net magnetization (Figure 2.9(ii)). Upon reversing the field, the FM spins try to follow the new field direction. If the magnetocrystalline anisotropy of the AFM is high and the interfacial AFM spins are strongly coupled to the AFM lattice, there will be no significant change in their alignment direction as the applied field tries to ferromagnetically align the FM spins with the AFM spins at the interface. As a result, the AFM spins at the interface exert a strong torque on the FM spins and the torque tends to keep them in their original position (Figure 2.9(iii)). The magnitude of the magnetic field required to completely reverse the FM layer would be larger when compared to the case of $T > T_N$, if it is coupled to an AFM because of the extra energy required to overcome the torque. However, if the applied field is reversed again to its initial direction (Figure 2.9(iv)), a smaller magnitude field compared to the case of $T > T_N$ would be required to rotate the FM spins since the torque exerted by the AFM spins is in the direction of the applied field (Figure 2.9(v)). A torque therefore acts on the FM spins from all angles except in the direction of the cooling field. The spins are thus said to have one single stable configuration which is in the direction of the cooling field, i.e., unidirectional anisotropy. The system behaves as if there was an extra (internal) biasing field, therefore, the FM hysteresis loop is shifted in the field axis generally opposite the direction of the cooling field and this shift is what is generally referred to as exchange bias [33, 34, 37].

Although this simple model provides an intuitive picture of exchange bias, there is little quantitative insight into the phenomenon due to the fact that the role of different parameters[3] involved in exchange bias such as anisotropy, interfacial roughness, spin configuration or magnetic domains, are still not well understood. As a result, the picture painted above may not be an applicable predictive model to all cases, hence our microscopic level understanding of exchange bias is still incomplete. Inspite of this, exchange bias has found niche industrial applications e.g., in magnetic recording, spin valve readback heads, and in MRAM memory circuits [33, 34].

---

[3] The different physical parameters needed to characterize an exchange biased system are treated in detail in the references.

2.4.2 Training effect

Another interesting dynamical property of exchange bias is observed in FM/AFM systems when they are cycled with a field [39, 40]. In many of these heterostructures, there is a gradual degradation of the exchange bias field (H_E) with the consecutive number of measurements of the hysteresis loop [39, 41–43]. The so-called "training effect" has been used to describe this aging phenomenon [41, 42]. Training effect is believed to originate from the irreversible changes that occur in the state and structure of the AFM layer in response to the dynamical environment [39, 41] and is generally more pronounced in polycrystalline AFM but very small or even nonexistent in single crystal-based exchange biased systems [41]. However, since a direct observation of an AFM metastable state has not been achieved due to the experimental difficulty in probing the magnetic configuration of the AFM layer [39]; the exact origin of the phenomenon is illusive [41].

Xi *et al.* [43] attributed exchange bias training effect to the change in the magnetic structure of the AFM layer as a result of of nucleation of the AFM domains when the biased system is swept with a reverse magnetic field. They obtained an analytical expression for the time dependence of the exchange field as [43]

$$H_e(t) = H_E\Big\{2\exp[-(t/\tau_D)^{\sigma}] - 1\Big\} \tag{2.26}$$

where H_E is the initial exchange field, τ_D is the characteristic relaxation time for exchange bias, and the power index $\sigma = 1/3$, in many cases. Pina *et al.'s* [44] study of nanocrystalline exchange-biased bilayers revealed a logarithmic time dependence of the the second and subsequent reversals of the exchange field upon switching off of the external field. They attributed this behavior to the evolution of the AFM surface in the magnetization reversal processes from a single wall motion process to multiple rotations due to large training effect. Dho *et al.* [41] also reported a logarithmic time relaxation behavior of the exchange bias field in exchange-coupled bilayers and concluded that the training effect was as a result of a thermally activated reversal of the AFM domain configuration in order to reduce the total magnetic energy. According to Binek *et al.* [42], the exchange bias training effect of all FM bilayer system (a system of exchange coupled bilayers of soft and hard FM thin films) is as a result of the deviation from equilibrium in the pinning layer. They derived an expression for the cycle dependent bias field for such an all FM bilayer system as

$$\mu_0 H_E(n) = (K+1)^{n-1}\left\{\mu_0 H_E(1) - K\mu_0 H_E^e\left[\frac{(K+1)^{n+1}-1}{K(K+1)^{n-1}} - (K+2)\right]\right\}, \tag{2.27}$$

where $H_E(n)$ is the bias field at n cycles, H_E^e is the equilibrium bias field, and K is the fitting parameter ranging from $-0.25 \leq K \leq -0.15$.

2.5 Interlayer exchange coupling

When two magnetic thin films (FM_1 and FM_2) are separated by a thin nonmagnetic spacer layer (NM), the magnetization of the layers couple to each other through the electrons of the spacer layer. This coupling, referred to as the interlayer exchange coupling (IEC), was first observed in 1986, in both transitional metal multilayers [Iron (Fe) films separated by a Chromium (Cr) layer] and rare-earth multilayers [Dysprosium (Dy) and Gadolinium (Gd) films separated by a Yttrium (Y) layer]. In the case of ferromagnetic thin films for example, Fe and Gd, the coupling results in parallel [ferromagnetic coupling, figure 2.10(a)] or antiparallel [antiferromagnetic coupling, figure 2.10 (b)] alignment of the magnetization at either side of the spacer layer, and the sign of the magnetization was found to oscillate as a function of the spacer thickness [45–47]. The magnetostatic coupling aligning the magnetizations antiparallel can arise due to the fringing fields at the edge of the sample when the lateral dimensions are sufficiently small. The antiparallel alignment results in the minimization of the fringing field energy. On the other hand, ferromagnetic interlayer coupling trying to align the magnetizations parallel can occur due to the local field produced by the interface roughness [47].

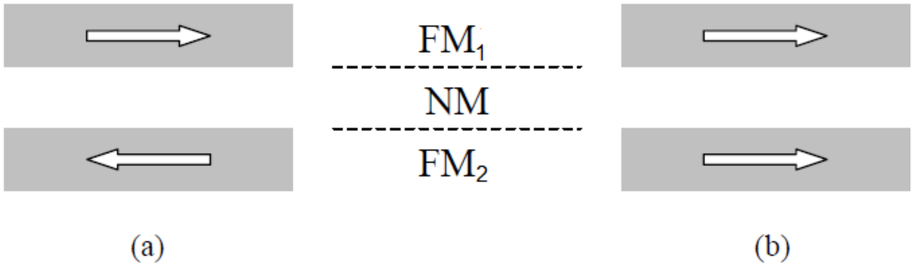

Figure 2.10: Schematic diagram illustrating the phenomena of (a)antiferromagnetic coupling and (b) ferromagnetic coupling between two ferromagnetic layers separated by a spacer layer. The arrows show direction of magnetization.

The exchange coupling energy per unit area is phenomenologically expressed as [47]:

$$E_i = -J_1 cos(\theta) - J_2 cos^2(\theta) \tag{2.28}$$

where θ is the angle between the magnetization of the two magnetic films on either side of the spacer layer, and the parameters J_1 and J_2 are determinants of the type and strength of the coupling. If the term with J_1 dominates, then it follows from the minima of Eq.(2.28) that the coupling is ferromagnetic when J_1 is positive and antiferromagnetic when it is negative. In the case of dominant and negative J_2, a $90°-$coupling is obtained. The first term of Eq.(2.28) is often called “bilinear” while the referred to as “biquadratic”. The biquadratic term is thought to originate from interfacial roughness [47].

Interlayer exchange coupling is an indirect interaction between magnetic layers mediated by the conduction electrons in the nonmagnetic magnetic layer. It is closely related to Ruderman-Kittel-Kasuya-Yoshida (RKKY) interaction between two magnetic impurities in a nonmagnetic host with the mediation role played by the conduction electrons in the host metal [45, 48, 49]. In other words, in the case of the RKKY interaction the localized impurities are coupled to each other by their influence on the electrons in the host while in the case of the IEC, the coupling between the two magnetic interfaces is achieved through the electrons in the spacer layer. Let us briefly consider the case of a single interface. The interface set up an oscillatory polarization in the nonmagnetic spacer layer; the polarization is therefore a single-particle effect. All electrons scatter from the interface and the probability densities of each electron results from the interference between the incoming and scattered waves. Since the interface is magnetic and the spin-up and spin-down electrons scatter differently from it, filling all states below the Fermi energy gives an oscillatory spin density. The contributions to the oscillatory spin density by the different waves are unequal since they have different wave vectors; hence periods. The different contributions cancel out except those at the Fermi energy as a result of the a sharp cut-off from the completely filled states to completely empty ones. The second interface then couples the spins density set up by the first. This coupling oscillates as a result of the oscillation of the spin density as a function of the thickness of the spacer layer [45].

2.6 Giant magnetoresistance effect

The giant magnetoresistance (GMR) effect describes the behavior of heterogeneous magnetic systems consisting of alternating layers of ferromagnetic and non-magnetic materials either in the form of multilayers or granular systems [13]. The effect describes the observation that the resistivity of layered magnetic structures is dependent on the relative alignment of the magnetization [47]. It is one of the most important discoveries in thin-film magnetism due to its tremendous technological potential and deep fundamental physics [50].

2.6.1 Phenomenological description

The discovery of GMR effect, by Baibich *et al.* [6] in 1988, was the first practical application of spintronics [4]. Baibich *et al.* observed that when Fe/Cr multilayer was subjected to an applied magnetic field, there was a significant reduction in the electrical resistance of the multilayer [6, 47, 50]. A similar but smaller magnitude of the effect was simultaneously observed in Fe/Cr/Fe trilayers and the effect has since been observed in other magnetic layered systems having Co, Fe or Ni as the ferromagnetic and Cr, Cu, Ag, or Au as the nonmagnetic spacer layer [50].

In the absence of an applied field, the thickness of the spacer layer was such that the adjacent Fe layers are aligned antiparallel due to antiferromagnetic interlayer coupling (cf. §2.5) across the Cr spacer layer. The application of a large enough external magnetic field saturates the sample and causes the magnetic moments of the Fe to align in a parallel configuration. The transition from antiparallel to parallel configuration leads to a reduction in the electrical resistance of the multilayer. The effect was much larger than either ordinary or anisotropic magnetoresistance; hence the name “giant magnetoresistance” [47, 50]. Figure 2.11 shows the variation in the resistance of the Fe/Cr multilayer measured by Baibich *et al.*

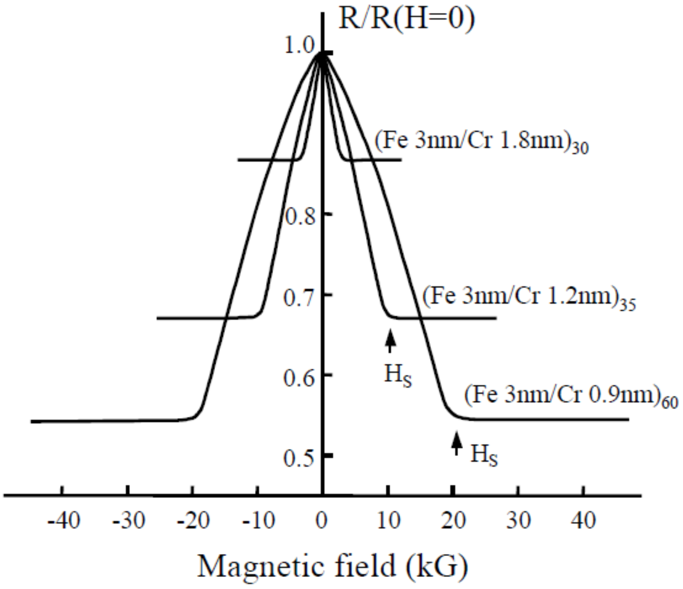

Figure 2.11: Normalized resistance versus applied magnetic field for several antiferromagnetically coupled Fe/Cr multilayer at 4.2 K. Arrows indicate the saturation field H_S, which required to overcome the antiferromagnetic interlayer exchange coupling between the Fe layers and align their magnetizations parallel. After [50].

If we denote the resistance for parallel (saturation field) and antiparallel (zero field) alignments by R_P and R_{AP} respectively, then the strength of the GMR effect is [2, 47]:

$$\frac{\Delta R}{R} = \frac{R_{AP} - R_P}{R_P}. \tag{2.29}$$

The magnetoresistance differs from structure to structure. Baibich *el al.* [6] observed up to 50% change in the resistance of the structure; Binasch *et al.* [8] observed a 1.5% change in the magnetoresistance of the Fe/Cr trilayer. Since the early observations, $\frac{\Delta R}{R}$ value as large as 150% has been observed in Cr/Fe/Cr superlattice by Fullerton *et al.* [51]. There have been instances where R_P has been observed to be high than R_{AP} resulting in a negative value for Eq.(2.29). This is referred to as “inverse GMR effect” [47].

The GMR effect experiments are performed in two principal geometries; the Current In Plane (CIP) and the Current Perpendicular to the Plane (CPP) [1, 2, 47, 50]. In the CIP geometry (figure 2.12(a)), the experiment is performed by measuring the electric field in the plane of the multilayer. Most of the current applications of GMR are based on this geometry [1, 50]. In the case of the CPP geometry (figure 2.12(b)), the experiment is performed by measuring the electric current perpendicular to the plane of the multilayer [50].

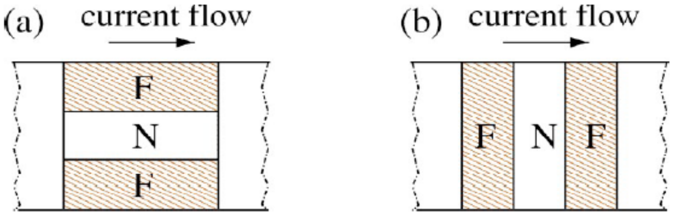

Figure 2.12: Schematic illustration of (a) the current in plane (CIP), (b) the current perpendicular to the plane (CPP) giant magnetoresistance geometry. After [1].

Although the relative effect is stronger in the CPP geometry compared to the corresponding magnitude in the CIP, measuring current in the CPP geometry present much challenge. The challenge arises from the extremely unfavorable geometric conditions; the very small thickness of the multilayer results in very low CPP resistance which is very difficult to detect without special structuring [2, 47, 50]. This obstacle can be overcome by using superconducting contacts (experiment possible only at low temperatures), by using techniques based on lithographically defined pillar structures, on magnetic multilayers grown on prestructured (grooved) substrates, or on electrodeposition of multilayer nanowires into the pores of an insulating polymer matrix [50]. In the structures mentioned, the GMR in the CPP geometry become strong enough for practical applications e.g., GMR based MRAM. Again the CPP geometry is easier to analyze theoretically whilst the experiment offers valuable insight about the physics of giant magnetoresistance since the CPP geometry is related to the tunneling magnetoresistance effect [1, 50].

GMR structures

The presence of an antiferromagnetic interlayer coupling is not a necessary requirement for GMR to occur. The antiferromagnetic alignment can also be achieved by using successive ferromagnetic layers with different coercivities (hysteresis effects). The magnetic moments of the soft and hard magnetic layers would respond to different magnitudes of the applied field. This provides a range over which the layers are antiparallel; hence have high resistance [50].

The use of spin valves is another option of changing the alignment of the magnetizations in the layers. The magnetization of one ferromagnetic layer in the spin valve is pinned by exchange coupling (cf. §2.4) to the adjacent antiferromagnetic layer, whereas the the magnetization of the other ferromagnetic layer is free to rotate when the external field is applied [47, 50]. Although the measured GMR values are higher in magnetic multilayers, most applications of GMR effect employ the spin valve because of the relatively small fields required to change the resistance [50].

Magnetic granular solids is another example of systems that exhibit GMR effect. The ferromagnetic precipitates in these materials are embedded in a non-magnetic host metal film. The applied magnetic field aligns the randomly-oriented magnetic moments of the precipitates leading to a reduction in the resistance of the granule [50]. Figure 2.13 shows the various types of systems in which GMR effect is observed.

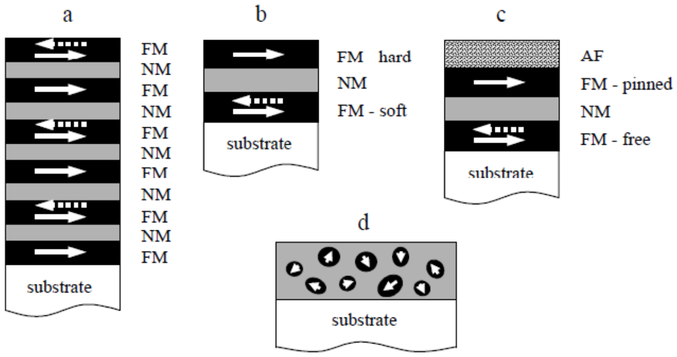

Figure 2.13: Various structures in which GMR can be observed: magnetic multilayer (a), pseudo spin valve (b), spin valve (c) and granular thin film [50].

2.6.2 The microscopic picture: spin dependent scattering

The mechanism leading to GMR can be qualitatively understood using Mott's "two current model" (briefly introduced in §1.1). The model is based on two main points proposed by Mott:

1. The electrical conductivity of metals can be described in terms of two independent conducting channels, which corresponds to the spin-up and spin-down electrons [1, 2, 5, 47, 50]. The spin-up and spin-down electrons are identified by their spins along the quantization axis. The probability of spin-flip scattering process occurring in metals is small compared to the probability of spin-conserved scattering process [5, 50]. In other words, the spin-up and spin-down electrons do not mix over long distances and as a result, the conductivity occurs in parallel for the two spin channels [1, 2, 5, 50].
2. The scattering rates for the spin-up and spin-down electrons in the ferromagnet differs irrespective of the nature of the scattering center [2, 5, 50]. This mobility difference between the two spin channels has its root in the exchange interaction which causes ferromagnetism itself [5]. According to Mott, the electric current is primarily carried by electron from the valence *sp* bands due to their low effective masses and high mobility. The *d* bands serve as the final states for the scattering of the *sp* electrons. In ferromagnets however, due to the exchange-splitting of the itinerant electron conduction *d* bands, the spin-up and spin-down electrons have different density of states at the Fermi energy [5, 50]. As a result, the scattering rates differ for the two conduction channels since the probability of scattering into these states is proportional to their densities [50].

Based on the above mentioned assumptions of Mott, let us analyze spin dependent scattering of electrons using the Pauli exclusion principle. If we assume that the scattering of electrons is elastic then according to the Pauli principle the electrons at the Fermi level (E_F) can only scatter into empty states near E_F. This means that the scattering probability is proportional to the density of states at E_F i.e., $D(E_F)$. Figure 2.14 shows the density of states of up-spin and down-spin orientations for Cu, Co and Fe. The Fermi level in Cu and other noble metals intersects only the conduction band whose density of states is low resulting in low scattering probability. The high conductivity of Cu (and other noble metals) is attributed to this. In contrast to noble metals, the *d* band in transitional metals is partially filled and the Fermi level intersects both the conduction and the *d* bands. Also the *d* levels are more localized and have high density of states compared to the outer *s* levels. This provides a new effective channel for scattering (Mott scattering) into the *d* band. This accounts for the poor conductivity observed in transitional metals. [2].

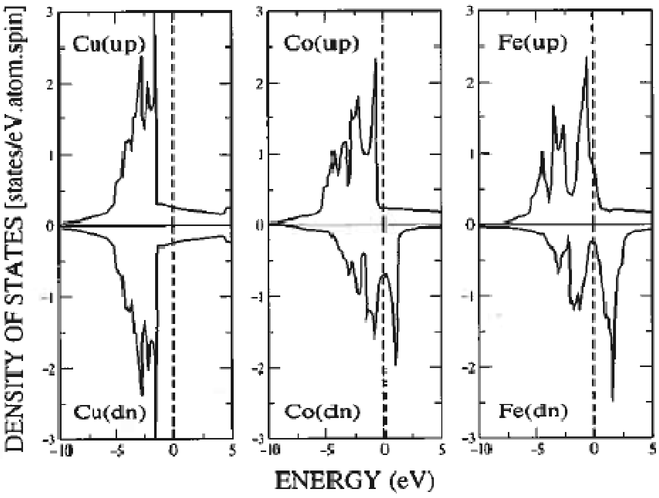

Figure 2.14: The density of states of copper, cobalt and iron. Broken line denotes the position of the Fermi level [2].

In ferromagnetic transitional metals, the *d* bands for up- and down-spin electrons are split by exchange interaction causing an almost rigid relative shift of the up- and down-spin *d* bands, shown in figure 2.14 for Co and Fe. In Co the up-spin *d* band is full corresponding a low density of states ($D^{\uparrow}(E_F)$), while the Fermi level of the down-spin band lies in the *d* and therefore the density of states ($D^{\downarrow}(E_F)$) is much higher. There is therefore an imbalance in the density of states for the up- and down-spin electrons in Co i.e., $(D^{\uparrow}(E_F)) \neq (D^{\downarrow}(E_F))$. This spin asymmetry in Co and other ferromagnetic transitional metals results in different scattering rates for the up- and down-spin electrons i.e., spin dependent scattering [2].

Mott's argument can be extended to explain the mechanism spin dependent scattering in GMR magnetic multilayers. In magnetic multilayers, electrons passing from a non-magnet spacer to a ferromagnet experience a potential barrier which is dependent on the electrons' spin orientation. This difference in the potential seen by up- and down-spin electrons in a ferromagnet is as a result of the exchange interaction. The spin dependent scattering at the ferromagnetic/non-magnetic interface due to the spin dependence of the scattering potentials is referred to as "interfacial spin dependent scattering". Figure 2.15 shows the band structure of Co, Cu, Fe and Cr in the [001] direction.

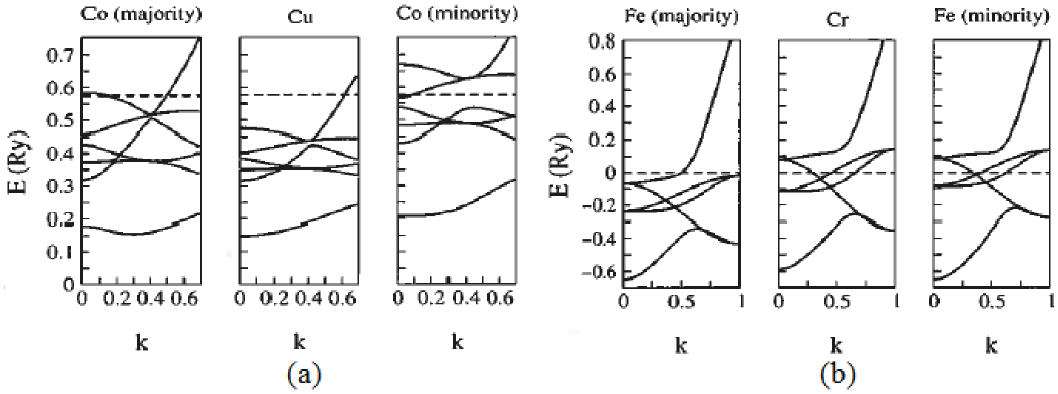

Figure 2.15: Band structures of (a) cobalt and copper along [001] direction in the vicinity of one of the Cu Fermi surface necks (b) iron and chromium in the [001[direction. Broken line denotes the position of the Fermi level [2].

The good match between the bands of Cu and the up (majority) spin band of Co observed in Figure 2.15(a) can lead us to conclude that an up-spin electron traversing the Cu/Co interface would encounter only weak scattering. The case of Cu and Co bands for the down (minority) spin electrons would give a different outcome because of the significant mismatch between the bands. A down-spin electron traveling across would therefore experience a strong scattering at the interface. Figure 2.15(b) shows a perfect match between Fe and the down-spin Cr bands and a mismatch with the up-spin bands [2].

Simple resistor model of GMR

We consider collinear magnetic configurations shown in Figure 2.16 and assume that the scattering is strong for electrons with spin antiparallel to the magnetization direction and weak for electrons with spin parallel to the magnetization direction to cater for the asymmetry in the density of states in accordance with Mott's second argument.

In the ferromagnetic configuration of the trilayer, the electrons with the up-spin experience a weak scattering in both the first and second ferromagnetic layers whilst the down-spin electrons experience strong scattering in both ferromagnetic layers. This is represented by two small up-spin channels and two large down-spin channels in Figure 2.16(a). Since conduction occurs in parallel in the two channels, the total resistance of the trilayer in its ferromagnetic configuration is determined by the low-resistance up-spin channel which shortens the high-resistance down-spin channel resulting in an overall low resistance. In the antiferromagnetic alignment of the trilayer both the up-spin and down-spin electrons are scattered strongly within one of the ferromagnetic layers and a weak scattering in the other. This is illustrated in Figure 2.16(b) by one large and one small resistor in each spin channel. This results in a high total resistance of the trilayer [2, 50].

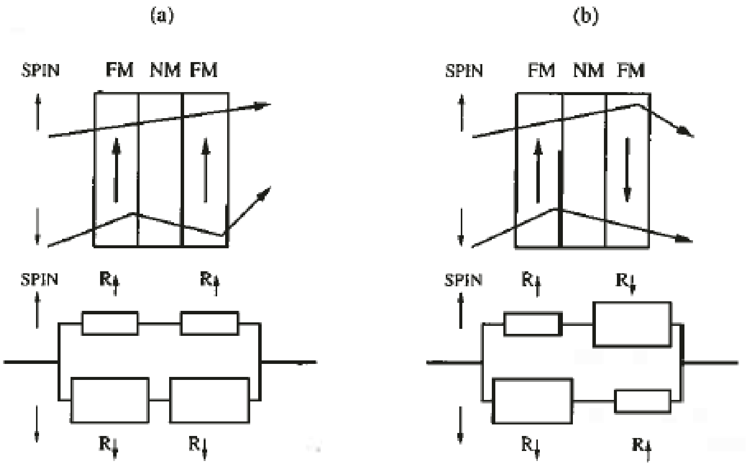

Figure 2.16: A resistor model of GMR [2].

The simple physical model presented above, though is believed to be correct, gives a primitive insight into the mechanism of GMR effect. It lacks the the quantitative explanation of the difference between the CIP and CPP geometries, the dependence of GMR material properties and layer thicknesses, and fails to emphasize on the critical role played by interfaces [2, 5].

2.7 Spin transfer torque effect

Giant magnetoresistance effect which involves the manipulation of the resistance of magnetic multilayers by an applied external field has provoked a lot of interest both in the academic research and industry. It has recently been realized that the magnets in magnetic multilayers can be excited through other means than external magnetic fields. In 1996 Slonczewski [10] and Berger [11] independently predicted a converse effect of GMR in which spin-polarized current could be used to manipulate the magnetic orientation in multilayers through exchange interaction [9, 12, 15, 27]. They predicted that in current perpendicular plane to the interface plane of spin-valve structures, a spin-polarized current in the right direction can excite and even reverse the magnetization of a magnetic layer [52]. This inverse phenomenon of current-driven excitations of magnetic multilayers has been called spin transfer torque (STT) effect [1, 9, 53]. The STT effect arises whenever the flow of spin-angular momentum through a sample is not constant; when a spin current created by spin filtering from one magnetic thin film is again filtered by a second magnetic thin film whose magnetization is not collinear with the first one. A portion of the spin-angular momentum is absorbed by the second magnet. The magnetization of the ferromagnet changes the flow of spin-angular momentum by exerting a torque[4] on the flowing electrons to reorient them. The flowing electrons must therefore exert an equal but opposite torque on the the ferromagnet. This torque, called the spin transfer torque, applied by the electrons on a ferromagnet is what excites or even reverses the magnetization of the ferromagnetic layer [27]. The first experimental evidence of the prediction was obtained by Tsoi *et al.* [15] and has since been amply confirmed by many other experimental findings [52, 53]. The huge interest STT effect has generated is largely due to the curiosity to understand the physics underlying the new phenomenon and its potential for device use: magnetization reversal of magnetic memories and magnetic media in which the magnetization reversal is achieved without an external magnetic fields. It also have potential application in spin-wave generation for production of high frequency radiations [53].

---

[4] defined as $\tau = dM/dt$

In the this section the STT effect is discussed beginning with the semiclassical treatment of the magnetization dynamics, followed by a description of Slonczewski's formulation of the spin-transfer model.

2.7.1 The Landau-Lifshitz-Gilbert equation

The Landau-Lifshitz-Gilbert (LLG) equation is a general equation describing the motion of magnetic moments in an externally applied field. When a magnetic configuration is subjected to an external field, the magnetization precesses around the instantaneous local effective field H_{eff}. If there is no damping, the magnetization distribution stays on a constant energy surface. Landau and Lifshitz in 1935 [54] introduced a phenomenological damping term into the equation of motion $dM/dt = -\gamma' M \times H_{eff}$:

$$\frac{dM}{dt} = -\gamma' M \times H_{eff} - \frac{\lambda}{M_s} M \times (M \times H_{eff}), \tag{2.30}$$

where λ is the Landau-Lifshitz damping parameter and M_s is the length of M. Gilbert [55] introduced a slightly different form of the damping term in 1955:

$$\frac{dM}{dt} = -\gamma M \times H_{eff} + \frac{\alpha}{M_s} M \times \frac{dM}{dt}. \tag{2.31}$$

Here, γ is the gyromagnetic ratio and α is the Gilbert damping parameter [24, 27, 52]. It should be stated that both forms of the damping parameter move the local magnetization vector towards the local effective direction. The two equations are known to be equivalent with the substitutions $\gamma' = \gamma/(1+\alpha^2)$ and $\lambda = \gamma\alpha/(1+\alpha^2)$ [27]. The effective field, H_{eff}, corresponds to the different contributions to the effective energy i.e., the applied-, exchange-, anisotropy-, and demagnetization field [52].

The first term of the LLG equation describes the Larmour precession of the magnetic moment at a fixed angle about the effective magnetic field direction. The second term describes the change of magnetic moment due to the damping torque causing the magnetic moment to turn toward the direction of H_{eff} when α is positive [24]. The precession and damping terms rotate the magnetization but do not change the length [27].

2.7.2 The spin transfer term

Let us consider a spin polarized current traveling through a F/N/F trilayer (e.g., a spin valve) as shown in Figure 2.17. Let us assume the magnetization of the second ferromagnetic layer (F_2) is pinned via interlayer coupling achieved by increasing its thickness compared to the first ferromagnetic layer (F_1). Again the thickness of the spacer layer is enough to prevent any significant exchange coupling between the ferromagnetic layers.

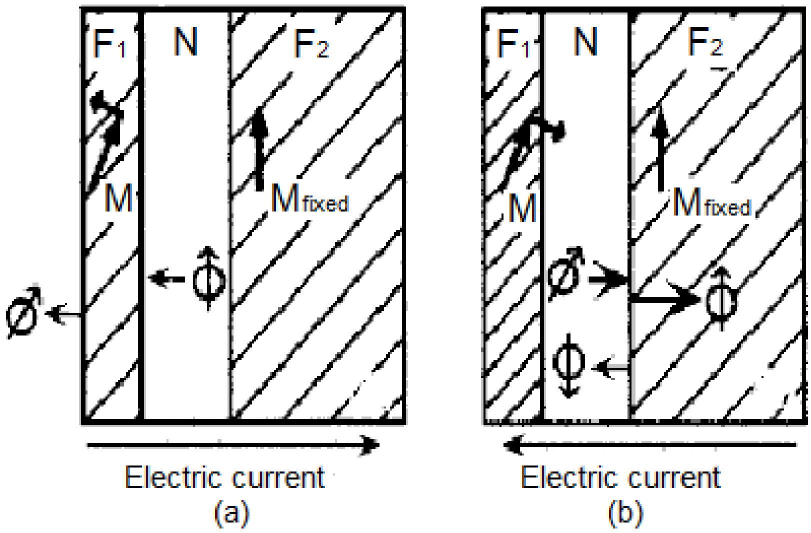

Figure 2.17: A schematic of spin-transfer model. (a) Electrons flowing from F_2 to F_1, initially polarized along the direction of magnetization $\hat{M}_{fixed}$, of F_2, exert torque on the magnetization $\hat{M}$, of F_1, which acts to align $\hat{M}$ with $\hat{M}_{fixed}$. (b) In the case of a current flowing in a reverse direction to (a), the electrons with spin antialigned with $\hat{M}_{fixed}$ will be reflected from F_2 and return to F_1 exerting a torque opposite to that in (a) which result in $\hat{M}$ turning away from $\hat{M}_{fixed}$. Antialigned configuration of the magnetizations is thus stable. After [56].

In the case of the right-flowing current (left-going electron flow as in Figure 2.17(a)) the electrons emerge from pinned layer, F_2, spin-polarized along the magnetization direction of that layer, $\hat{M}_{fixed}$. Slonczewski showed that when this spin-polarized electron current impinge on the unpinned layer (F_1) they exert a torque on its magnetic moments $\hat{M}$ tending to align them in the direction of the current ($\hat{M}_{fixed}$). The parallel alignment of the two ferromagnetic layers is then the stable configuration. Assuming the conservation of angular momentum, Slonczewski showed that the torque generated on the magnetic moments is as a result of the deposition of the perpendicular portion of the angular momentum carried by the incident electrons into the magnetic layer and the magnitude of the torque is proportional to the spin-polarized current that acts to align the moment along the polarization of the incident current [10, 56]. The impact of the torque on the free layer magnetization $\hat{M}$ due to the misalignment with the fixed layer magnetization $\hat{M}_{fixed}$ is accounted for by adding an extra term to the LLG equation:

$$\frac{dM}{dt}_{STT} = \eta(\theta)\frac{\mu_B I}{e\nu}\hat{M} \times (\hat{M} \times \hat{M}_{fixed}), \tag{2.32}$$

where I is the spin polarized current, ν is the free-layer volume on which the spin torque acts, $\eta(\theta) = q/(A + B\cos\theta)$ i.e., depends on the misalignment between the two magnetization directions, M and $\hat{M}_{fixed}$ are unit vectors in the direction of $\hat{M}$ and $\hat{M}_{fixed}$ respectively, and $\cos(\theta) = \hat{M} \cdot \hat{M}_{fixed}$ [10, 27].

If the direction of flow of the current is reversed (right-going electron flow as in Figure 2.17(b)) the electron current now emerges from F_1 polarized along $\hat{M}$. As a result of the large thickness of F_2, when current scatter off it, only the portion of the spin-polarized current that is parallel to $\hat{M}_{fixed}$ will be transmitted while the antiparallel portion will be reflected back to F_1. The reflected minority electrons then exert a torque opposite to the direction of the first case (shown in figure 2.17(a)) according to the symmetry in Eq. (2.32) i.e. the $\sin\theta$ symmetry of the spin transfer torque effect. The torque therefore rotate $\hat{M}$ away from $\hat{M}_{fixed}$ making the antiparallel alignment the stable configuration. The instability can take the form of a dynamical precession (spin-wave) or a moment switch to a stable antiparallel orientation [10, 56].

Equation (2.32) is of similar form as the Landau-Lifshitz damping terms and hence the Gilbert damping term. Combining the LLG equation [Eq.(2.31)] and the STT term [Eq.(2.32)] we obtain:

$$\frac{dM}{dt} = -\gamma M \times H_{eff} + \frac{\alpha}{M_s} M \times \frac{dM}{dt} + \eta(\theta)\frac{\mu_B I}{e\nu}\hat{M} \times (\hat{M} \times \hat{M}_{fixed}). \tag{2.33}$$

By equating the last two terms of Eq.(2.33) to zero and solving for I, one obtains two critical values of the current. A positive value of the current (I_c^+) is obtained for the switch from an initial parallel alignment of the magnetic orientation $(\theta = 0)$, whereas a negative value (I_c^-) is found for the switching from an initial antiparallel alignment $(\theta = \pi)$ [57].

2.7.3 Spin transfer torques in antiferromagnets

We already know from § (2.1.2) that antiferromagnets are spontaneously magnetized below a critical Néel temperature at which point the magnetic moments of two (or more) sublattices are in opposite directions to each other resulting in a zero net magnetization. In the absence of the possibility of manipulating the strongly coupled antiferromagnetic moments with an external magnetic field, the STT phenomenon offers a way to excite the antiferromagnetic order parameter since the electric current is polarized on the atomic scale

[58]. Núñez *et al.* [59] and Haney *et al.* [60] predicted the existence of current-induced torques in circuits made up of only antiferromagnetic elements based on theoretical studies [61]. Haney *et al.* predicted a strong enough current-induced torques that could switch the antiferromagnetic order parameter at current densities orders of magnitude (~ 100) smaller than the switching current densities of ferromagnetic metal circuits [60]. Núñez *et al.* attributed the small current densities in the antiferromagnetic circuits to the absence of shape anisotropy in antiferromagnets and also that the spin transfer torques in antiferromagnets is a bulk effect compared to the interface effect found in ferromagnetic systems [59].

Wei and others [62] reported changes in the exchange bias field of a spin valve as function of the direction of current flow when an FeMn/CoFe/Cu/CoFe exchange-biased spin valve [CoFe as the FM layer, FeMn as the AFM layer and Cu as the non-magnetic spacer layer] was injected with a high-density electric current from a point contact. The observed increase or decrease in the bias depending on the direction of the current could not be explained by the conventional STT effect observed in ferromagnetic layers. They attributed it to the current-induced torque acting on the AFM component of the spin valve structure and also predicted that the effect could be exploited in the magnetic states of spin valve devices such as in magnetic memory applications.

2.8 Point contact measurements

The use of point contacts as a spectroscopy tool in the study of the transport properties of metals has become a standard technique in solid-state physics [63]. Propelled into prominence by Yanson [64] for studying electron-phonon interaction, point contact spectroscopy is now applied in many kinds of electron scattering mechanisms with different kinds of elementary excitations in metals [63, 65].

In order to study the nano-scale properties of magnetic nanostructures, a point contact is formed by pressing a probe onto the structure. The properties of the resulting electrical contact depend strongly on the ratio of the radius of contact (a) to the electron mean free path (l). Comparing these two characteristic parameters results in three possible regimes [63, 65].

If the contact radius is much smaller than the electron mean free path distance, i.e., $a << l$, the electron transport is not Ohmic but “ballistic” or “clean”. A voltage, V, applied over the contact will accelerate each electron ballistically through the contact, gaining an energy, eV, within the distance, l, where, e, is the electron charge [63, 65, 66]. The point-contact resistance for such an electron transport was calculated by Sharvin [67]:

$$R_s = \frac{4\rho l}{3\pi a^2}, \tag{2.34}$$

where ρ is the resistivity of the material under study. For a pure ballistic contact, scattering events within the contact is assumed to be insignificant and the Sharvin resistance R_s is independent of l since $\rho = 1/l$ [63, 66].

In the limit of very short mean free path, i.e., $a >> l$, referred to as the "thermal", "dirty" or "Maxwell" regime [65], the electron transport through the contact is inhibited by multiple scattering within the contact [63, 65]. The resistance to such a flow was calculated by Maxwell [68]:

$$R_M = \frac{\rho}{2a}. \tag{2.35}$$

In contrast with the ballistic regime where the energy of the electron is lost over a large distance from the constriction, the lose of energy in the thermal regime occurs in the contact area resulting in an increase in temperature at the centre of the contact (Joule heating) [65].

In the intermediate range, between the ballistic and the thermal regimes, the Sharvin and Maxwell expressions are not valid. By interpolation of the two limiting resistances Wexler [70] obtained:

$$R = \frac{4\rho l}{3\pi a^2} + \Gamma(K)\frac{\rho}{2a} = \frac{4\rho l}{3\pi a^2}\left[1 + \frac{3\pi}{8}\Gamma(K)\frac{a}{l}.\right] \tag{2.36}$$

Here $K = a/l$ is the Knudsen number, and $\Gamma(K)$ is a slowly varying function of K, with $K(0) = 1$ and $K(\infty) = 0.694$ [63, 65, 66]. Since the factor $\Gamma(K)$ is of order of unity, the point contact resistance can be seen as a series resistance of a ballistic part (the Sharvin value, Eq. 2.34) and a diffusive part (the Maxwell value, Eq. 2.35) [63].

If the electron flow through a ballistic contact without scattering, the contact resistance is expressed by the Sharvin formula, the current-voltage characteristic of the metallic constriction will be linear (Ohm's law) and the second derivative d^2V/dI^2 of the voltage with respect to the current will be zero [71]. However, experimental results have produced a non-linear $I - V$ characteristic for such a contact and the second derivative shows structures that have been found to coincide with structures in the phonon density of states of the metal being studied [65, 66]. This observation has proven to be a very useful technique for fundamental study of scattering in metals [66].

The voltage derivative (d^2V/dI^2) of the Wexler resistance [Eq.(2.36)] also generates structures that correspond to typical phonon frequencies of the metal under study. The structures are due to the Maxwell term [second term of Eq.(2.36)] because of the energy dependence of the electron mean free path. The Sharvin term [first term of Eq.(2.36)] is independent of the electron mean free path since the product ρl is constant for a given metal [66].

Chapter 3

Experimental Setup and Method

3.1 Instrumentation

The point contact measurement was performed using a coaxial probe. The sample was mounted on an acrylic platform and a magnetic field was applied using an electromagnet which was also mounted on the platform. The electromagnet was connected to an external power supply (Kepco BOP 100-10MG). Figure 3.1 is a schematic diagram of the circuit used for measuring the point contact resistance.

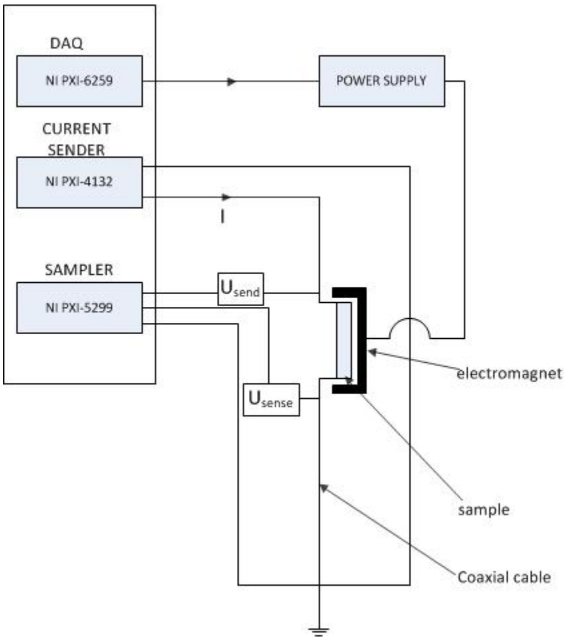
DAQ
NI PXI-6259
POWER SUPPLY
CURRENT SENDER
NI PXI-4132
I
SAMPLER
NI PXI-5299
U_send
U_sense
electromagnet
sample
Coaxial cable

Figure 3.1: A schematic diagram of the circuit used for measuring the contact resistance.

The measurement of the contact resistance was controlled by a program written in $LabVIEW$; a programming environment from National Instruments (NI). The data acquisition was undertaken with a National Instrument PXI [5] system (NI PXI-8187) and a standard desktop computer. The PXI system was responsible for setting measurement parameters, undertaking measurements etc.; and the computer was for displaying the host program to the probe and for data processing after the experiment.

In the experiment we utilized three extension cards of the PXI system (NI PXI-8187). The three extension cards are of different forms from the main motherboard module which is also of the same form factor as the PXI extension cards.

1. A multifunction DAQ (NI PXI-6259) having four 16 bit input channels, four 16 bit digital to analog output channels, 48 digital input/output (I/O) lines and several trigger lines. The card was used to measure the sense voltage of the power supply to the electromagnet.
2. The second card, the current sender (NI PXI-4132), had two analog input channels. One of these input channels was used to send current to the sample via the probe.
3. The third card, the sampler (NI PXI-5299), is essentially a high speed DAQ having two unbalanced coaxial input channels. The two channels can be used to acquire signals in the range of ± 5 V up to a selectable resolution of 24 bits at up to 500 kSamples/s. These two channels were used to measure the send (u_1) and the sense (u_2) voltage from the current sender to- and from the sample respectively [69].

3.1.1 Electromagnet and current source

The electromagnet used consisted of two home-made Helmholtz coils with approximately 850 winds each ($N \simeq 850$). The separation between them was just enough to permit the mounting of the platform on which the sample was placed (shown in Figure 3.2). The electromagnet was connected to a high performance voltage controlled Kepco BOP 100-10MG current source. The current source is capable of both sinking and sourcing operation of 10 A at 100 V up to frequencies of 4 Hz. The coils produce field of $H \simeq 100$ mT in the center region at the maximum current of 10 A [69].

3.2 Sample

The sample studied in this thesis is a spin valve structure consisting of Ta (3 nm)/FeMn (8 nm)/Co (3 nm)/Cu (3 nm)/$Fe_{20}Ni_{80}$ (3 nm)/Cu (10 nm)/Si (001). It was prepared by magnetron sputtering at a base pressure of 2×10^{-5} Pa and a deposition pressure of 0.3 Pa. The Si here is used as a substrate; the 10nm Cu was used to stimulate fcc (111) growth of

---

[5] The PXI system is a technology standard for instrumentation hardware which stands for "PCI eXtensions for Instrumentation" where the PCI refers to "Peripheral Component Interconnect" [72].

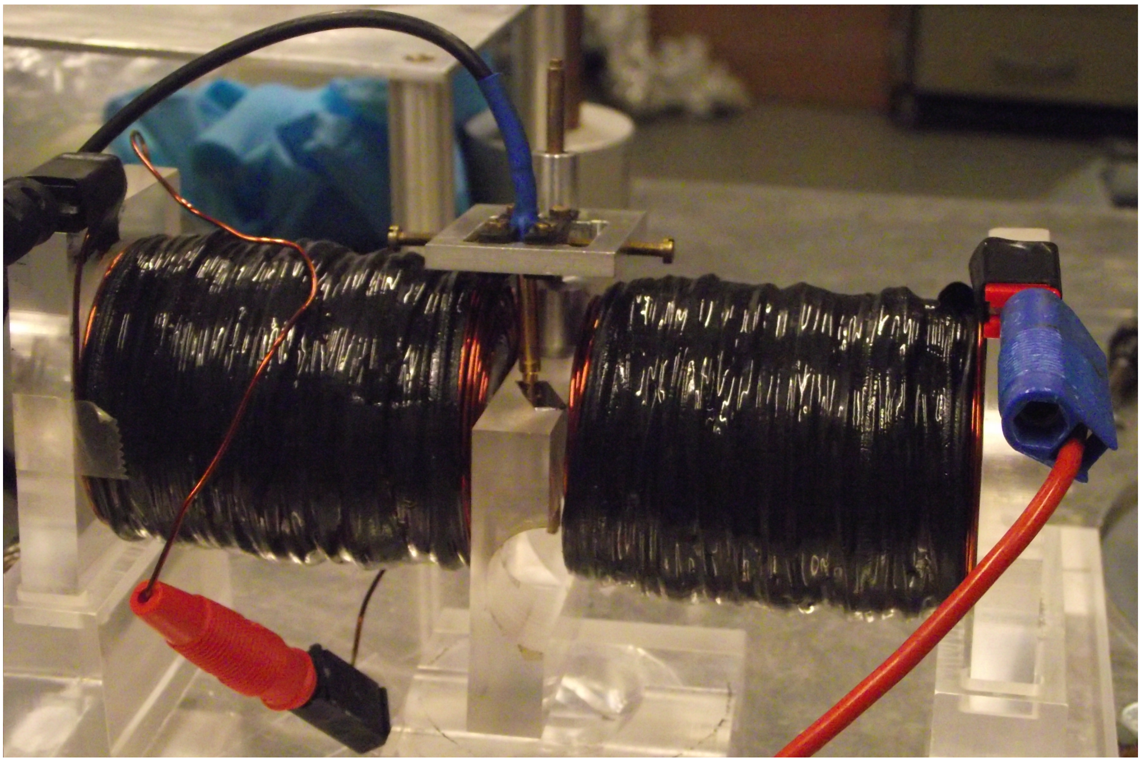

Figure 3.2: The experimental setup of the point-contact resistance measurement. The sample is placed on a rectangular acrylic platform in-between the two Helmholtz coils. The different parts of the setup are tightly held together so that the system acts as one unit.

FeMn and also to enhance exchange bias; Co and FeNi are the ferromagnetic layers; the antiferromagnetic layer FeMn is pinned to Co layer via exchange bias effect; and Ta is the metallic capping layer. The exchange bias at the FeMn-Co interface was calibrated to be 270 Oe.

3.3 Experimental method

The experimental setup is shown in Figure 3.2 and Figure 3.1 shows the circuit for measuring the the contact resistance. Also shown in Figure 3.1 are the control (u_{send}) and the measured (u_{sense}) signals. The point-contact resistance measurements were performed at room temperature with a coaxial probe. The probe was adjusted until there was a good contact between the probe's tip and the sample.

In order to study the the recovery and relaxation behavior of the spin valve structure, magnetoresistance measurements were performed by simultaneously applying a constant current through the tip of the probe perpendicular to the sample plane while sweeping the sample repeatedly with a magnetic field in a direction parallel to the sample plane. The source of the magnetic field was the home-made Helmholtz coils. The magnetic field was swept in the form of a triangular wave at a sampling rate of 100 k/s and was stopped with an interval time t_{off},which varied from 0.01 to 5 s. For each time interval, the procedure was repeated for different field scan rates ranging from 1050 to 13500 Oe/s. The data obtained from the experiment was analyzed using matlab.

Chapter 4

Results and Discussion

4.1 Giant Magnetoresistance

The giant magnetoresistance (GMR) measurements of the FeNi/Cu/Co/FeMn spin valve structure was undertaken at standard conditions of temperature and pressure. Figure 4.1 shows typical magnetoresistance (MR) curves obtained when the spin valve structure was swept with a magnetic field in the form of a triangular wave at a field scan rate of 13500 Oe/s for 5 *s*.

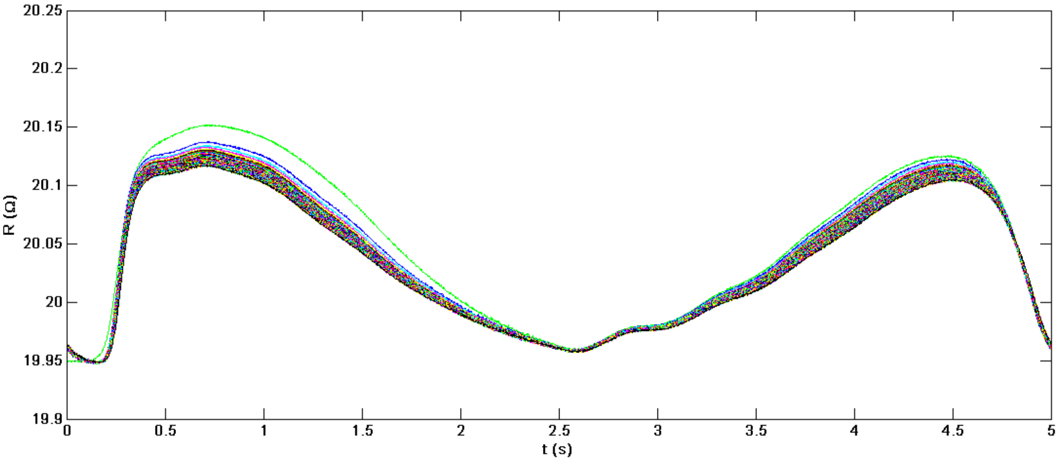

Figure 4.1: Typical magnetoresistance curves obtained when a 4 A current was sent through the sample while being swept with a triangular wave at a field scan rate of 13500 Oe/s.

As a result of the pinning effect of FeMn on the Co layer, the hysteresis loops of the Co layer are shifted and fully separated from the hysteresis loops of the FeNi layer in all the MR curves obtained in our measurements. We can therefore study the switching behavior of both Co and FeNi layers from the MR curves. Also, the shapes and positions of the MR curves of the Co layer changes with the number of field cycles but that of the FeNi remains unchanged throughout the experiment [38].

From Figure 4.1 the MR curve of the first hysteresis loop (green) is distinct from the curves of the second and subsequent hysteresis loops. This is due to the asymmetry in the first magnetization reversal. The onset of the first peak in the GMR curve is as a result of the reversal of the free FM layer (FeNi); the first drop results from the reversal of the pinned FM layer (Co) when the exchange bias field is overcome; the second peak has its origin in the repinning of the exchange biased layer; and second drop results from the ferromagnetic interlayer coupling of the free layer again to the (re)pinned layer.

4.2 Exchange bias and training effect

In order to study the exchange bias and its training effect in our spin valve structure, several measurements of consecutive hysteresis loops similar to that in section 4.1 were performed. The current through the sample was kept constant while the sample was swept with a magnetic field in the form of a triangular wave for T_{on} seconds; the field was turned off for T_{off} seconds; and then turned back on for another T_{on} seconds. The measurements was repeated for different field scan rates; 13500, 5400, 2700, 1350, and 1080 Oe/s. Figures 4.2-4.7 are exchange field (H_E) versus number of field cycles (n) plots for part of a series of measurements with a field scan rate of 5400 Oe/s, $T_{on} = 5s$, and varying T_{off}. For each Figure $n = 1$ to $n = 50$ represent the first field sweep for $T_{on} = 5\ s$, and $n = 51$ to $n = 100$ is the second field sweep for $T_{on} = 5\ s$ after the field has been turned off for T_{off} seconds. The yellow vertical column in Figure 4.2 represents the period when the field sweep was stopped for T_{off} seconds.

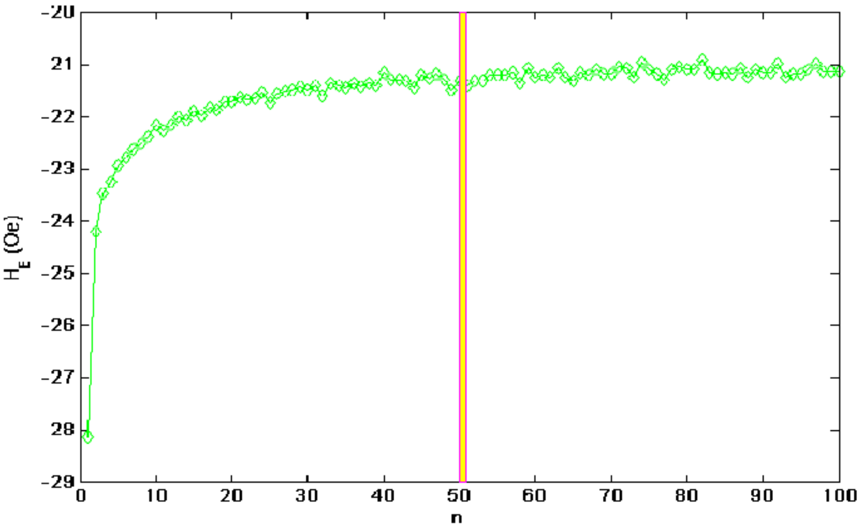

Figure 4.2: An H_E versus n where the magnetic field was turned off after $T_{on} = 5\ s$ for $T_{off} = 0.01\ s$, then turned back on for another $T_{on} = 5\ s$.

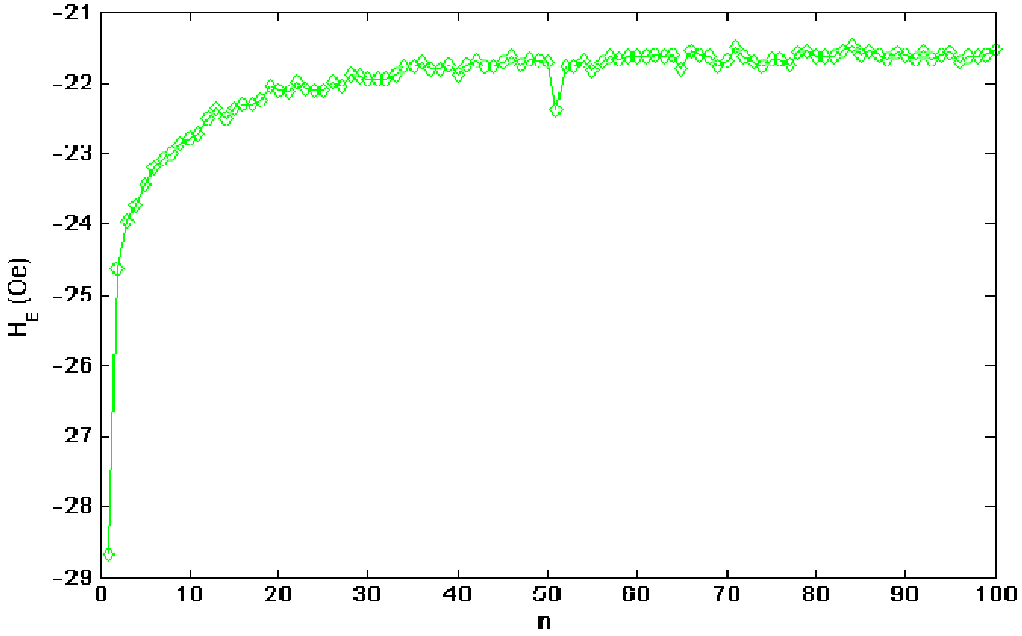

Figure 4.3: An H_E versus n where the magnetic field was turned off after $T_{on} = 5\ s$ for $T_{off} = 0.05\ s$, then turned back on for another $T_{on} = 5\ s$.

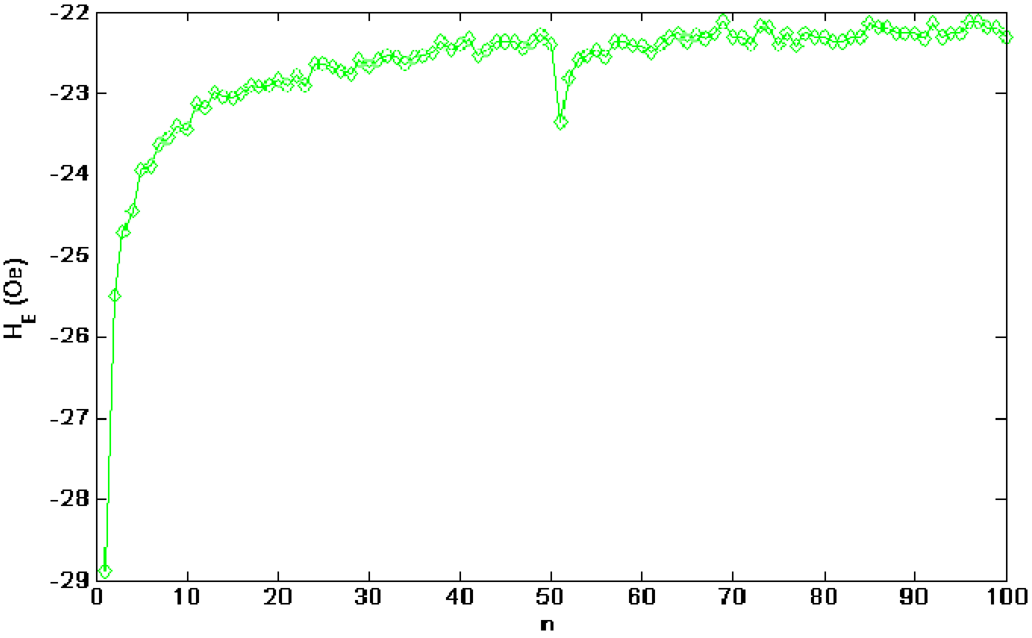

Figure 4.4: An H_E versus n where the magnetic field was turned off after $T_{on} = 5\ s$ for $T_{off} = 0.1\ s$, then turned back on for another $T_{on} = 5\ s$.

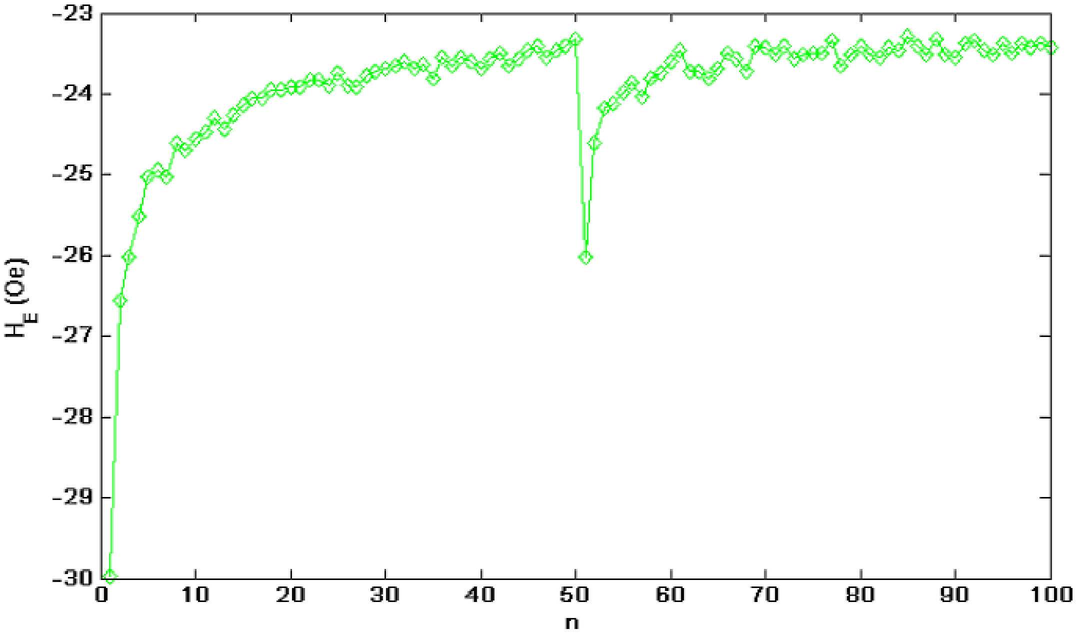

Figure 4.5: An H_E versus n where the magnetic field was turned off after $T_{on} = 5$ s for $T_{off} = 0.5$ s, then turned back on for another $T_{on} = 5$ s.

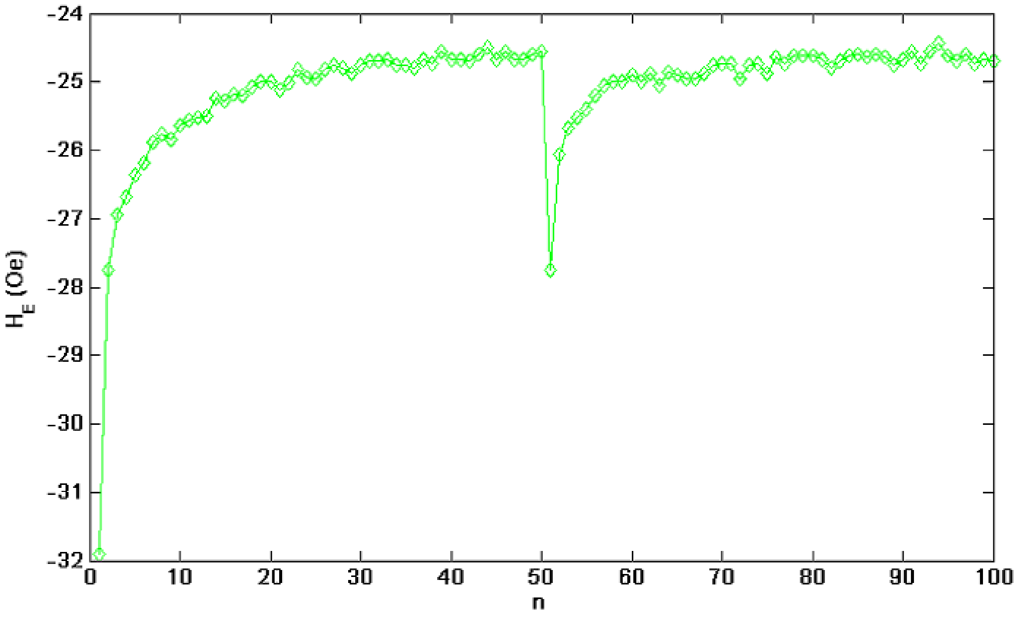

Figure 4.6: An H_E versus n where the magnetic field was turned off after $T_{on} = 5$ s for $T_{off} = 1$ s, then turned back on for another $T_{on} = 5$ s.

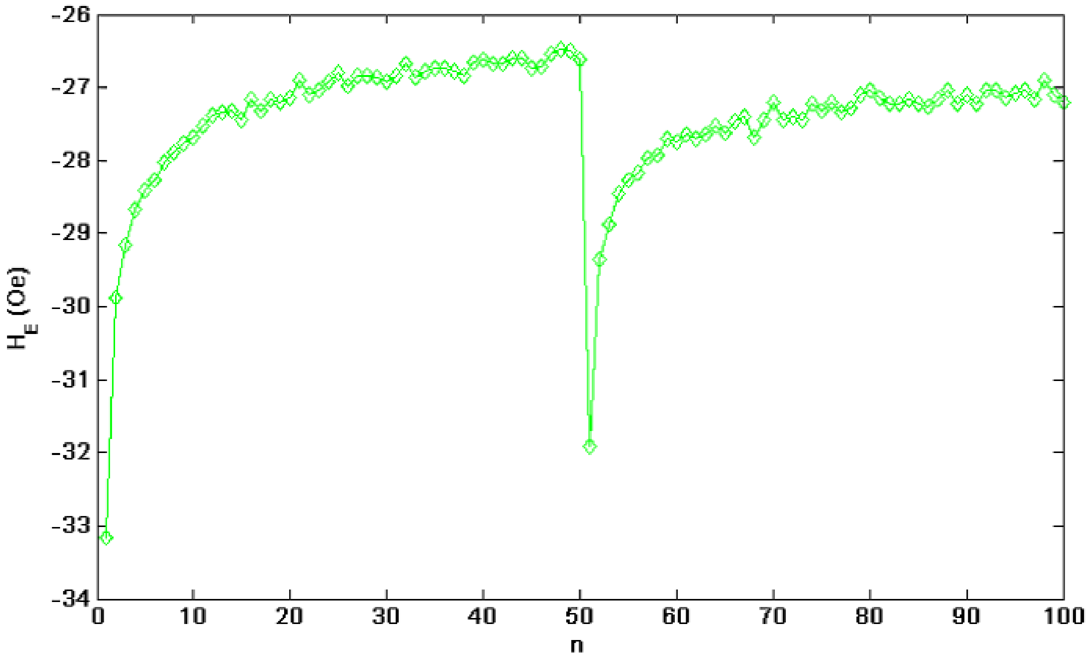

Figure 4.7: An H_E versus n where the magnetic field was turned off after $T_{on} = 5\ s$ for $T_{off} = 5\ s$, then turned back on for another $T_{on} = 5\ s$.

It is evident in all cases that the exchange field generally decreases with increasing number of cycles, and there is a significant partial recovery ($n = 51$) when the field sweep is stopped for T_{off} seconds. This is consistent with an earlier observation by Dho *et al.* [41] although our measurement time scale is much shorter. Generally the longer the T_{off}, the stronger the recovery of the exchange field H_E; an almost zero recovery is observed in Figure 4.2 where the field sweep was stopped for just 0.01 s.

It can be observed from the H_E versus n plots (Figures 4.2-4.7) that H_E gradually decreases with increasing n in all cases with the exception of the first points ($n = 1$) where there are sharp decreases. According to Chan *et al.* [73] the large decrease in H_E occurring between $n = 1$ and $n = 2$, followed by a more gradual decrease for the subsequent loops is an indication that the training effect is composed of two distinct mechanisms. The first hysteresis loop is asymmetric compared to the second and subsequent loops; the first magnetization reversal of the first hysteresis loop has an abrupt jump while the second reversal is gradual (i.e., magnetization reversal asymmetry). Both experimental and simulation results have shown that during the first magnetization reversal, the pinned FM layer develops domains that are oriented parallel or antiparallel to the applied field while in the subsequent reversals, the magnetization rotates usually perpendicular to the applied field. Hence the observed magnetization reversal asymmetry in the first hysteresis loop does not occur in the second and subsequent hysteresis loops and therefore these loops are symmetric [74]. When the H_E versus n curves are fitted by $1/\sqrt{n}$, $\ln(n)$, and $e^{-\alpha n}$ (Figure 4.8), the $1/\sqrt{n}$ relation is found to produce the best fit with the exception of $n = 1$ in agreement with Refs. [73, 75]. This is further confirmed by the H_E versus $n^{-1/2}$ plot in Figure 4.9. As can be seen, the data does adhere to this form reasonably well with the exception of data point $n = 1$, in agreement with Ref. [75].

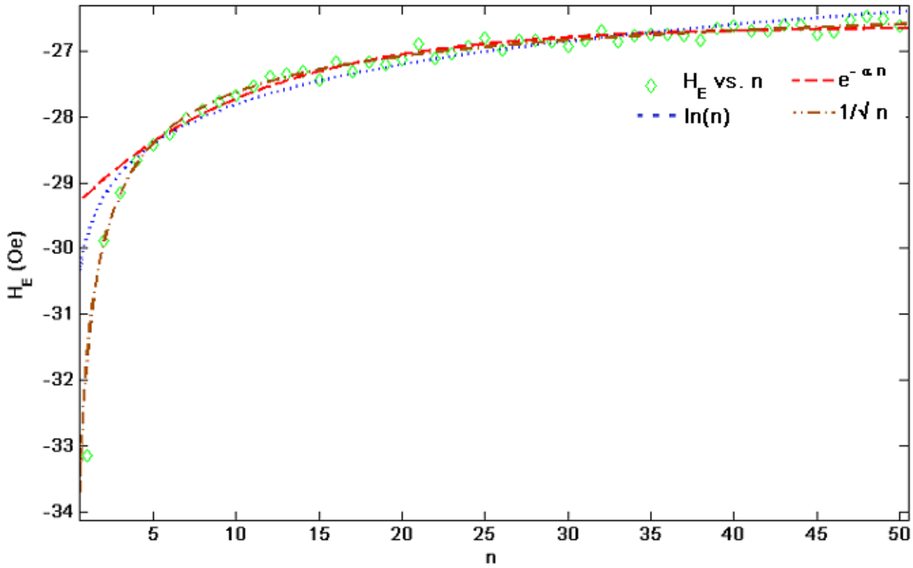

Figure 4.8: Exchange field H_E versus number of field cycles n. The red dash, blue dot, and brown dash-dot lines are respectively $e^{-\alpha n}$, $\ln(n)$, and $1/\sqrt{n}$ fits to the data.

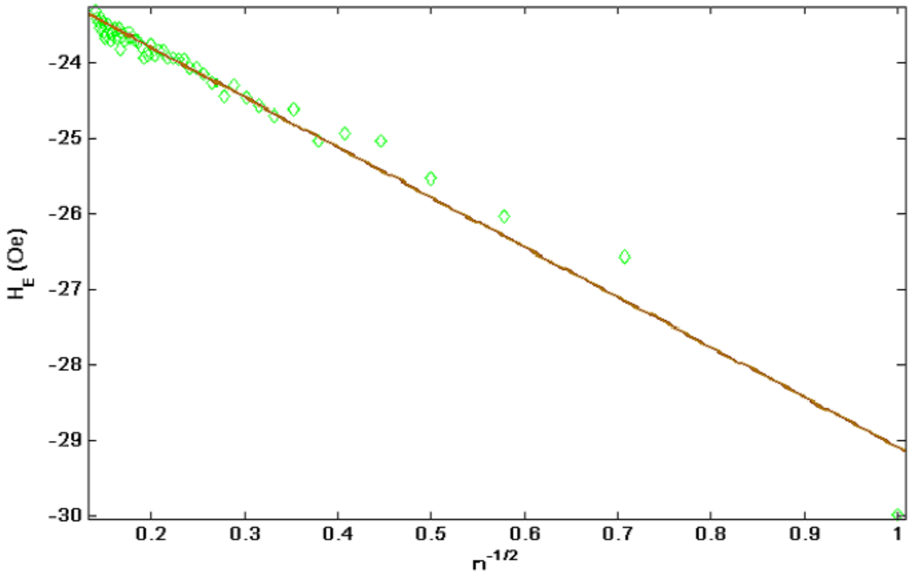

Figure 4.9: Exchange field H_E versus number of field cycles $n^{-1/2}$. The data shows a reasonable adherence to this form.

In order to further study the recovery speed of the training effect, the recovery ratio , R, of the training effect as a function of the interval time , t_{off}, at different field scan rates was measured. The recovery ratio of the exchange field is defined as [38]:

$$R = \left[\frac{H_E^A - H_E^B}{H_E^F - H_E^B} \right] \times 100\%, \tag{4.1}$$

where H_E^F is the exchange field for the first GMR sweep; H_E^B is the exchange field for the last GMR sweep just before the field was turned off; and H_E^A is the exchange field just after the recovery. Figure 4.10 shows the plots of R as a function of t_{off} for the different field scan rates. The solid lines are linear fits of R to the $\log(t_{off})$.

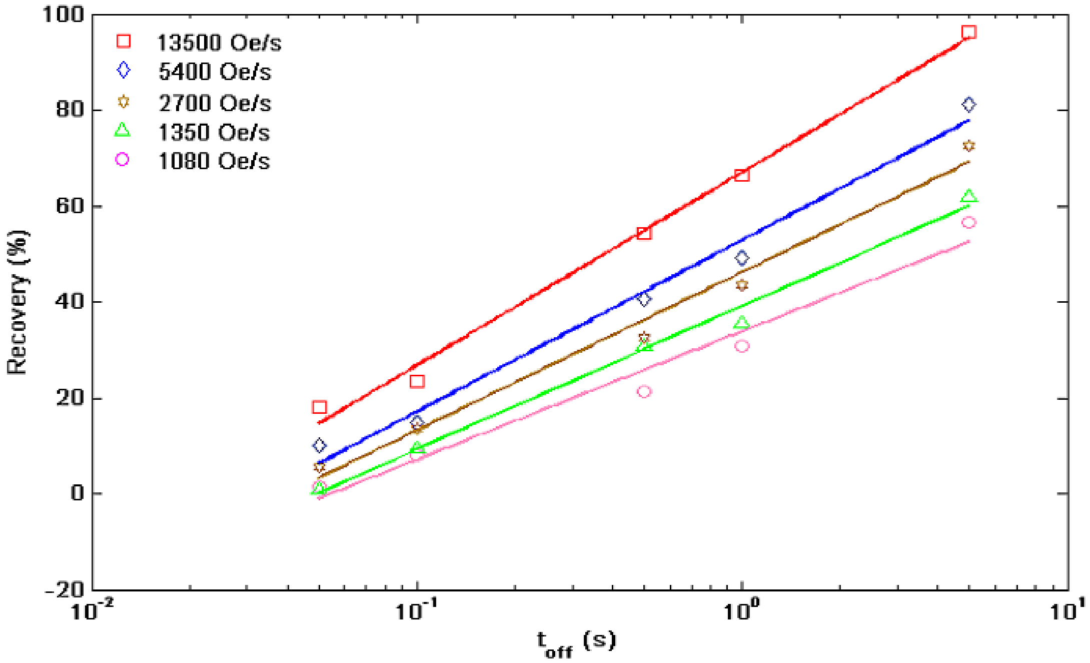

Figure 4.10: The percentage recovery of the exchange field H_E as a function of the interval time (t_{off}) for different field scan rate. The solid lines are linear fits of a $\log(t_{off})$ function.

It is evident from Figure 4.10 that the recovery ratio R increases with increasing interval time t_{off}. The linear fits of R to the $\log(t_{off})$ exhibit a strong proportionality relation. Again for a fixed interval time t_{off}, the corresponding value of R increases with increasing field scan rate. The means that the recovery speed of H_E increase with increasing scan rate. This observation is in agreement with earlier observations made by Yang *et al.* [38] in Co/Cu/FeNi/FeMn spin valve and Dho *et al.* [41] in FeNi/FeMn bilayers although our recovery speed is several orders of magnitude faster than that of Ref. [41]. The increase of R with increased scan rate goes to suggest that the observed recovery in the H_E versus n curves for scan rates higher than 5400 Oe/s is expected to be swift than those observed in Figures 4.2-4.7. The opposite of this also holds.

Figure 4.11 shows the slopes and intercepts of the fits in Figure 4.10 as a function of the field scan rates. The solid lines are linear fits to the logarithm of the field scan rate. The slopes are seen to vary slightly with the field scan rates whilst the intercept greatly increase with increasing field scan rate.

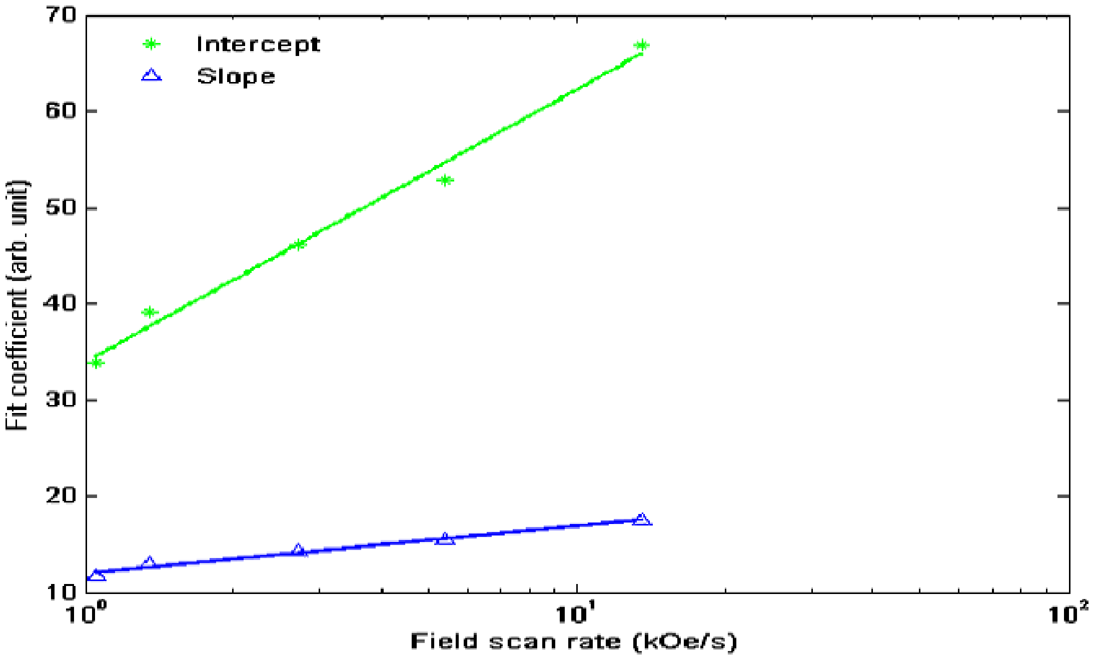

Figure 4.11: The slope and intercept of the fits in Figure 4.10 as a function of the field scan rates. The solid lines are linear fits to the logarithm of the field scan rate.

The linear regression for the fits in Figure 4.10 is of the form

$$R = a\ln(\nu_\sigma t_{off}) + b, \quad c, \tag{4.2}$$

where ,a, and ,b, are regression coefficients; ν_σ is a characteristic frequency called the attempt frequency, assumed here to be unity for convenience; and ,c, is the mean square error of the regression. For the different scan rates we have

$$\begin{aligned}
13500 \text{ Oe/s}: &\quad R = 17.474\ln(t_{off}) + 66.907 \quad c_1 = 0.99696\\
5400 \text{ Oe/s}: &\quad R = 15.538\ln(t_{off}) + 52.779 \quad c_2 = 0.99335\\
2700 \text{ Oe/s}: &\quad R = 14.312\ln(t_{off}) + 46.130 \quad c_3 = 0.99291\\
1350 \text{ Oe/s}: &\quad R = 12.984\ln(t_{off}) + 39.079 \quad c_4 = 0.99638\\
1050 \text{ Oe/s}: &\quad R = 11.628\ln(t_{off}) + 33.821 \quad c_5 = 0.98608
\end{aligned}$$

The error margins in our fits can be estimated in percentages as $(1-c)\times\%$. The percentage errors are 0.304, 0.665, 0.709, 0.362, and 1.392% respectively for 13500, 5400, 2700, 1350, and 1050 Oe/s.

As noted earlier, the recovery speed ,R, of the exchange field ,H_E, increases with increasing interval time ,t_{off},. Also the at a fixed t_{off}, R is found to increase with increasing field scan rate. We can therefore assume that the regression coefficients ,a, and ,b, are dependent on both t_{off} and and the field scan rate. The time required for the total relaxation τ of the exchange bias can be estimated by defining:

$$\tau = t_{off}(\delta = 100) - t_{off}(\delta = 0). \tag{4.3}$$

From Eq.(4.2)

$$t_{off} = \frac{1}{\nu_\sigma}\exp\left(\frac{R-b}{a}\right), \tag{4.4}$$

$$\tau = \frac{1}{\nu_\sigma}\left[\exp\left(\frac{100-b}{a}\right) - \exp\left(\frac{-b}{a}\right).\right] \tag{4.5}$$

The relaxation time τ are 6.62, 20.85, 43.10, 109.02, and 297.24 s for 13500, 5400, 2700, 1350, and 1050 Oe/s respectively. The relaxation time is thus found to decrease with increasing scan rate indicating that the energy distribution of the antiferromagnet is affected by the magnitude of the scan rate. This has been attributed to the narrowing of the energy distribution of the antiferromagnet's active domains [38].

We have already seen from Figures 4.2-4.7 that the exchange field gradually decrease with increasing field cycles. This is a macroscopic indication of a configurational rearrangement of the spin structure towards equilibrium [76]. We also saw in Figure 4.8 that the H_E versus n plots were fitted best by the $1/\sqrt{n}$ relation compared to $\ln(n)$ and $e^{-\alpha n}$. We now follow the theoretical approach of Binek *et al.* [42, 76] in modeling our result. The time evolution of the interface magnetization of the antiferromagnetic layer S is given by

$$\xi \frac{dS}{dt} = -\frac{\partial \Delta F}{\partial S}, \tag{4.6}$$

where ξ is a phenomenological damping constant and ΔF is the nonequilibrium free energy of the pinning layer. In its simplest form, ΔF characterizes the change of the free energy from its equilibrium. If we assume that $\Delta F(\partial S) = \Delta F(-\partial S)$, a series expansion of ΔF up to the fourth order in ∂S is

$$\Delta F = \frac{1}{2}a(\partial S)^2 + \frac{1}{4}b(\partial S)^4 + O(\partial S)^6, \tag{4.7}$$

where the powers of the order $O(\partial S)^6$ are negligible if $|\partial S|$ is sufficiently small. Exponential relaxations, which is generally faster than other potential decays, are typically observed when spin correlation becomes negligible. Exchange bias requires large antiferromagnetic spin correlation in other to pin the ferromagnetic layer during its magnetization reversal. Since exchange bias and training effect disappear above the blocking temperature (i.e., the temperature at which thermal stability occurs for a given exchange biased system [77]) where the antiferromagnetic spin correlation significantly diminishes, a nonexponential relaxation is expected below the blocking temperature; this requires that $a = 0$. Evaluating Eq. (4.6) with a free energy expression with a 4^{th} order leading term yields $1/\sqrt{n}$ relaxation of the system.

The strong $\log(t)$ dependence of the recovery speed of H_E seen in Figure 4.10 is an indication of a thermally activated reversal process that involves a range of activation energies in the antiferromagnet [38, 41]. The recovery and relaxation of the exchange bias with high field scan rate could therefore be modeled using the thermal activation spectrum model, originally introduced for relaxation in amorphous metals [41]. The change in the exchange bias ΔH_E is expressed in terms of the antiferromagnet's activation energy $q(E)$ as

$$\Delta H_E = q(E) k_B T (\nu_\sigma t). \tag{4.8}$$

According to Eq.(4.8), the slopes in Figure 4.11 are functions of the antiferromagnet spin configuration which is independent of the the field scan rate. The slopes are therefore expected to remain unchanged with varying scan rate as was the case in the results of Ref. [38]. Since the calculated error margins from our fits are much smaller, the small variations of the slopes with changing field scan rate observed in Figure 4.11 can be attributed to the short delay time between successive measurements. Yang *et al.* [38] attributed the large variation of the intercept with the high scan rate to the time delay due to the different field scan speeds.

Chapter 5

Conclusion

5.1 Conclusion

High field scan rate (1050-13500 Oe/s) studies of the recovery and relaxation of the exchange bias in Co/Cu/FeNi/FeMn spin valve has been conducted. Measurements were performed by simultaneously applying a constant current to the sample through the tip of the coaxial probe while sweeping the sample repeatedly with an external magnetic field in the form of a triangular wave. The exchange bias field (H_E) versus the number of field cycles (n) curves were found to be best fitted by the $1/\sqrt{n}$ relation in agreement with Chan *et al.* [73] and Lund and Leighton [75], as against the $\ln(n)$ dependence obtained by Yang *et al.* [38] in the same sample. A recovery of the exchange bias when the field cycling is stopped has been observed and the recovery ratio (R) is found to be a function of the logarithm of the recovery time ($\log(t)$) in agreement with both Yang *et al.* and Dho *et al.* [41]. For a fixed interval time, the recovery was observed to increase with increasing field scan rate. The relaxation time (τ) of the exchange bias has estimated to be 6.62, 20.85, 43.10, 109.02, and 297.24 s for 13500, 5400, 2700, 1350, and 1050 Oe/s respectively showing a decrease of τ with scan rate. The $1/\sqrt{n}$ dependence of H_E and the $\log(t)$ dependence of R have been discussed using thermal activation model.

5.2 Suggestions for future work

The present experiment was done on a single sample. We suggest that further work be done on samples with varying antiferromagnet thickness in order to investigate the dependence of the training effect and its recovery ratio on this parameter (AFM thickness) at high scan rate. We again suggest that the experiment be repeated for a fixed thickness at different ambient temperatures in other to investigate temperature dependence of the measured dynamic behaviors at high field scan rates.

Bibliography

[1] I. Žutić, J. Fabian, and S. Das Sarma. Spintronics: Fundamentals and applications. *Rev. of Mod. Phys.,* 76:323-408, 2004.

[2] M. Ziese and M. J. Thornton, editors. *Lecture notes in Physics: Spin Electronics.* Springer Verlag, Heidelberg, 2001.

[3] S. A. Wolf, D. D. Awschalom, R. A. Buhrman, J. M. Daughton, S. von Molnár, M. L. Roukes, A. Y. Chtchelkanova, and D. M. Treger. Spintronics: A spin-based electronics vision for the future. *Science,* 294:1488-1495, 2001.

[4] J. Lu, K. G. West, J. Yu, W. Yin, D. M. Kirkwood, L. He, R. Hull, S. A. Wolf, and D. M. Treger, editors. *Nanoscale magnetic materials and applications: Spintronics and novel magnetic materials for advanced spintronics.* Springer Verlag, Heidelberg, 2009.

[5] J. F. Gregg, I. Petej, E. Jougguelet, and C. Dennis. Spintronics- a review. *J. Phys. D: Appl. Phys.,* 35:R121-R155, 2002.

[6] M. N. Baibich, J. M. Broto, A. Fert, F. Nguyen Van Dau, and F. Petroff. Gaint magnetoresistance of (001)Fe/(001)Cr magnetic superlattices. *Phys. Rev. Lett.,* 61(21):2472-2475, 1988.

[7] G. A. Prinz. Magnetoresistance. *Science,* 282:1660-1663, 1998.

[8] G. Binasch, P. Grüberg, F. Saurenbach, and W. Zinn. Enhanced magnetoresistance in layered magnetic structures with aniferromagnetic interlayer exchange. *Phys. Rev. B,* 39(7):4828-4830, 1989.

[9] A. Kalitsov, M. Chshiev, I. Theodonis, N. Kioussis, and W. H. Butler. Spin-transfer torque in magnetic tunnel junctions. *Phys. Rev. B,* 79:174416-174427, 2009.

[10] J. Slonczewski. Current-driven excitation of magnetic multilayers. *Journal of Magnetism and Magnetic Materials,* 159:L1-L7, 1996.

[11] L. Berger. Emission of spin waves by a magnetic multilayer traversed by current. *Phys. Rev. B,* 54(13):9353-9358, 1996.

[12] Y. Huai. Spin-transfer torque MRAM (STT-MRAM). *AAPPS Bulletin,* 18(6):33-40, 2008.

[13] C. L. Dennis, R. P. Borges, L. D. Buda, U. Ebels, J. F. Gregg, M. Hehn, E. Jouguelet, K. Ounadjela, I. Petej, I. L. Prejbeanu, and M. J. Thornton. The defining length scales of mesomagnetism: a review. *J. Phys.: Condens. Matter,* 14:R1175-R1262, 2002.

[14] V. Cros, O. Boulle, J. Grollier, A. Hamzić, M. Muñoz, L. G. Pereira, and F. Petroff. Spin transfer torque: a new method to excite or reverse a magnetization. *C. R. Physique,* 6:956-965, 2005.

[15] M. Tsoi, A. G. M. Jansen, J. Bass, W.-C. Chiang, M. Seck, V. Tsoi, and P. Wyder. Excitation of a multilayer by an electric current. *Phys. Rev. Lett.,* 80(19):4218-4284, 1998.

[16] E. B. Myers, D. C. Ralph, J. A. Katine, R. N. Louie, and R. A. Buhrman. Current-induced switching of domains in magnetic multilayer. *Science,* 285:867-870, 1999.

[17] A. P. Guimarães. *Magnetism and magnetic resonance in solids.* Wiley, New York, 1998.

[18] R. E. Hummel. *Electronic properties of material.* Springer Verlag, New York, 2001.

[19] B. D. Cullity and C. D. Graham. *Introduction to magnetic materials.* Wiley, Hoboken, 2009.

[20] J. M. D. Coey. *Magnetism and magnetic materials.* Cambridge University Press, New York, 2010.

[21] É. du Trémolet de Lancheisserie, D. Ginnoux, and M. Schlenker editors. *Magnetism-Fundamentals.* Springer, Boston, 2005.

[22] M. Saxegaard. *Scanning tunneling microscopy based point-contact measurements of nanoscale magnetic systems.* PhD thesis, NTNU, Trondheim, Norway, 2010.

[23] J. D. Patterson and B. C. Bailey. *Solid-state physics: Introductory to the theory.* Springer Verlag, Berlin Heidelberg, 2007.

[24] J. Stöhr and H. C. Siegmann. *Magnetism- From fundamentals to nanoscale dynamics.* Springer Verlag, Berlin Heidelberg, 2006.

[25] A. Hubert and R. Schäfer. *Magnetic domains.* Springer Verlag, Berlin Heidelberg, 1998.

[26] W. F. Jr. Brown. *Micromagnetics.* Wiley, New York, 1963.

[27] D. C. Ralph and M. D. Stiles. Spin transfer torques. *Journal of Magnetism and Magnetic Materials,* 320:1190-1216, 2008.

[28] H. Kronmüller and M. Fähnle. *Micromagnetism and the microstructure of ferromagnetic solids.* Cambridge University Press, Cambridge, 2003.

[29] S. Blundell. *Magnetism in condensed matter.* Oxford University Press, London, 2001.

[30] C. Kittel. Physical theory of ferromagnetic domains. *Rev. of Modern Phys.,* 21(4):541-583, 1949.

[31] A. A. Minakov, I. V. Shvets, and V. G. veselago. Magnetostriction and antiferromagneic domains dynamics in helical antiferromagnets. *Journal of Magnetism and Magnetic Materials,* 88:121-133, 1990.

[32] A. Scholl, J. Stöhr, J. Lüning, J. W. Seo, J. Fompeyrine, H. Siegwart, J.-P. Locquet, F. Nolting, S. Anders, E. E. Fullerton, M. R. Scheinfein, and H. A. Padmore. Observation of antiferromagneic domains in a epitaxial thin films. *Science,* 287:1014-1016, 2000.

[33] E. A. Berkowitz and K. Takano. Exchange anisotropy-a review. *Journal of Magnetism and Magnetic Materials,* 200:552-570, 1999.

[34] J. Nogués and I. K. Schuller. Exchange bias. *Journal of Magnetism and Magnetic Materials,* 192:203-232, 1999.

[35] W. H. Meiklejohn and C. P. Bean. New magnetic anisotropy. *Phys. Rev.,* 105(3):904-913, 1957.

[36] M. Kiwi. Exchange bias theory. *Journal of Magnetism and Magnetic Materials,* 234:584-595, 2001.

[37] W. H. Meiklejohn. Exchange anisotropy. *J. of Applied Phys.,* 33(3):1328-1335, 1962.

[38] D. Z. Yang, A. Kapelrud, M. Saxegaard, E. Wahlström, and S. M Zhou. High field scan rate dynamic behaviour of the exchange bias in Co/Cu/FeNi/FeMn spin valves. to be published.

[39] T. Hauet, J. A. Borchers, P. Mangin, Y. Henry, and S. Mangin. Training effect in an exchange bias system: the role of interfacial domain walls. *Phys. Rev. Lett.,* 96:067207-067211, 2006.

[40] W. H. Meiklejohn. Characterization and analysis of the training effect of exchange bias in couupled Ni/IrMn bilayers. *J. of Applied Phys.,* 101:09E513-09E515, 2007.

[41] J. Dho, C. W. Leung, and M. G. Blamire. Universal time relaxation behavior of the exchange bias in ferromagnetic/antiferromagnetic bilayers. *Journal of Applied Phys.,* 99:033910-033914, 2006.

[42] C. Binek, S. Polisetty, X. He, and A. Berger. Exchange bias training effect in coupled all ferromagnetic bilayer structures. *Phys. Rev. Lett.,* 96:067201-067204, 2006.

[43] H. Haiwen, S. Franzen, S. Mao, and R. M. White. Exchange bias relaxation in magnetic fields. *Phys. Rev. B,* 75:014434-014438, 2007.

[44] E. Pina, C. Prados, and A. Hernando. Large training effects in magnetic relaxation and anisotropic magnetoresistance in nanocrystalline exchange-biased $Ni_{80}Fe_{20}$/Co-O bilayers. *Phys. Rev. B,* 69:052402-052405, 2004.

[45] M. D. Stiles. Interlayer exchange coupling. *Journal of Magnetism and Magnetic Materials,* 200:322-337, 1999.

[46] T. Katayama, S. Yuasa, J. Velev, M. Ye. Zhuravlev, S. S Jaswal, and E. Y. Tsymbal. Interlayer exchange coupling in Fe/MgO/Fe magnetic tunnel junctions. *Applied Phys. Lett.,* 89:112503-112505, 2006.

[47] R. Waser, editor. *Nanoelectronics and information technology.* Wiley, Second edition, 2005.

[48] P. Bruno. Theory of interlayer magnetic coupling. *Phys. Rev. B,* 52(1):411-439, 1995.

[49] P. M. Haney, C. Heiliger, and M. D. Stiles. Bias dependence of magnetic interactions: application to interlayer exchange coupling in spin valves. *Phys. Rev. B,* 79:054405-054413, 2009.

[50] E. Y. Tsymbal and D. G. Pettifor. Prospectives of giant magnetoresistance. *Solid State Physics,* 56:113-237, Academic Press, 2001.

[51] E. E. Fullerton, M. J. Conover, J. E. Mattson, C. H. Sowers, and S. D. Bader. 150% magnetoresistance in sputtered Fe/Cr(100) superlattices. *Applied Phys. Lett.,* 63(12):1699-1701, 1993.

[52] Y. Tserkovnyak, A. Brataas, G. E. W. Bauer, B. Halperin. Nonlocal magnetization dynamics in ferromagnetic heterostructures. *Rev. of Modern Phys.,* 77:1375-1421, 2005.

[53] J. Bass, S. Urazhdin, N. O. Birge, and W. P. Pratt. Current-driven excitations of magnetic multilayers: a brief reveiw. *Phys. Stat. Sol.,* 7:1379-1385, 2004.

[54] L. Landau and E. Lifshitz. On the theory of the dispersion of magnetic permeability in ferromagnetic bodies. *Phys. Z. Sovietunion,* 8, 153-169, 1935.

[55] T. L. Gilbert. A Lagrangian formulation of gyromagnetic equation of the magnetization field. *Phys. Rev.,* 100:1243, 1955.

[56] E. B. Myers, D. C. Ralph, J. A. Katine, F. J. Albert, and R. A. Buhrman. Point-contact studies of current-controlled domain switching in magnetic multilayer. *Journal of Applied Phys.,* 87(5):5502-5504, 2000.

[57] J. A. Katine, F. J. Albert, R. A. Buhrman, E. B. Myers, and D. C. Ralph. Current-driven magnetization reversal and spin-wave excitations in Co/Cu/Co pillars. *Phys. Rev. Lett.,* 84(14):3149-3152, 2000.

[58] Y. Xu, S. Wang, and K. Xia. Spin-transfer torques in antiferromagnetic metals from first principle. *Phys. Rev. Lett.,* 100:226602-226605, 2008.

[59] A. S. Núñez, R. A. Duine, P. Haney, and A. H. MacDonald. The theory of Spin torques and giant magnetoresistance in antiferromagnetic metals. *Phys. Rev. B,* 73:214426-214434, 2006.

[60] P. M Haney, D. Waldron, R. A. Duine, A. S. Núñez, H. Guo, and A. H. MacDonald. *Ab initio* giant magnetoresistance and current-induced torques in Cr/Au/Cr multilayers. *Phys. Rev. B,* 75:174428-174434, 2007.

[61] P. M Haney and A. H. MacDonald. Current-induced torques due to compensated antiferromagnets. *Phys. Rev.* 100:196801-196805, 2008.

[62] Z. Wei, A. Sharma, A. S. Núñez, P. M Haney, R. A. Duine, J. Bass, A. H. MacDonald, and M. Tsoi. Changing exchange bias in spin valves with an electric current. *Phys. Rev. Lett.,* 98:116603-116606, 2007.

[63] H. M. Swartjes, A. G. M. Jansen, and P. Wyder. Magnetoresistance of metallic point contacts. *Phys. Rev. B,* 38(12):8114-8120, 1988.

[64] I. K. Yanson. *Sov Phys.-JETP* 39:506, 1974.

[65] A. M. Duif, A. G. M. Jansen, and P. Wyder. Point-contact spectroscopy. *J. Phys.: Condens. Matter,* 1:3157-3189, 1989.

[66] A. G. M. Jansen, A. P. van Gelder, and P. Wyder. Point-contact spectroscopy in metals. *J. Phys. C: Solid St. Phys.,* 13:6073-6118, 1980.

[67] Y. V. Sharvin. *Sov Phys.-JETP,* 21:655, 1965.

[68] J. C. Maxwell. *A treatise on electricity and magnetism.* Clarendon, Oxford, 1904.

[69] A. Kapelrud. *A scanning tunneling microscope for point contact investigations of magnetodynamics in FeMn/FeNi bilayers* MSc. thesis, NTNU, Trondheim, Norway, 2009.

[70] G. Wexler. The effect and the non-local Boltzmann transport equation in orifice and disk geometry. *Proc. Phys. Soc.,* 89:927-941, 1966.

[71] Yu. G. Naidyuk and I. K. Yanson. Point-contact spectroscopy. *arXiv:physics/0312016v1,* 2003.

[72] PXI System Alliance. *PXI Hardware Specification,* revision 2.1, www.pxisa.org, 2003.

[73] M. K Chan, J. S. Parker, P. A. Crowell, and C. Leighton. Identification and seperation of two distinct contributions to the training effect in polycrystalline Co/FeMn bilayers. *Phys. Rev. B,* 77:014420-014424, 2008.

[74] A. Hoffmann. Symmetry driven irreversibility at ferromagnetic-antiferromagnetic interfaces. *Phys. Rev. Lett.,* 93(9):097203-097206, 2004.

[75] M. S. Lund and C. Leighton. Interplay between reversal asymmetry, training, and induced anisotropy in epitaxial exchange-biased bilayers. *Phys. Rev. B,* 76:104433-104438, 2007.

[76] C. Binek. Training of the exchange bias effect: A simple analytic approach. *Phys. Rev. B,* 70:014421-014424, 2004.

[77] X. Y. Lang, W. T. Zheng, and Q. Jiang. Dependence of the blocking temperature in exchange biased ferromagnetic/antiferromagnetic bilayers on the thickness of the antiferromagnetic layer. *Nanotechnology,* 18:155701-155706, 2007.